Journal of Quantitative Spectroscopy & Radiative Transfer 110 (2009) 808–832

Contents lists available at ScienceDirect

Journal of Quantitative Spectroscopy & Radiative Transfer

journal homepage: www.elsevier.com/locate/jqsrt

Review

Electromagnetic scattering by nonspherical particles: A tutorial review

Michael I. Mishchenko *

NASA Goddard Institute for Space Studies, 2880 Broadway, New York, NY 10025, USA

ARTICLE INFO

Article history:
Received 2 October 2008
Received in revised form
3 December 2008
Accepted 18 December 2008

Keywords:
Electromagnetic scattering
Nonspherical particles
Polarization

ABSTRACT

This tutorial review is intended to provide an accessible and self-contained introduction to the discipline of electromagnetic scattering by nonspherical particles and discuss the most general ways in which the scattering and absorption properties of particles and small random particle groups are affected by particle morphology. The main focus is on how nonsphericity influences our way of describing and quantifying electromagnetic scattering by particles and how it is likely to affect, both qualitatively and quantitatively, the principal theoretical descriptors of scattering and the relevant optical observables. Several quantitative examples included in this review are the result of a controlled laboratory measurement or a numerically exact theoretical computation and are intended to illustrate the main theses and conclusions.

Published by Elsevier Ltd.

Contents

* Tel.: +1 212 678 5590; fax: +1 212 678 5622.
E-mail address: mmishchenko@giss.nasa.gov

0022-4073/$ - see front matter Published by Elsevier Ltd.
doi:10.1016/j.jqsrt.2008.12.005

1. Introduction

In his famous paper of 1908, Mie [1] developed a comprehensive theory of electromagnetic scattering by a perfectly spherical homogeneous particle and used it to explain several experimental facts pertaining to the optics of colloidal gold [2]. A small discrepancy between the measured and calculated polarization was interpreted by Mie as a residual effect of nonsphericity of the gold microparticles (see Fig. 1a). The final sentence of his paper reads: "For the sake of completeness of the theory, it is absolutely necessary to investigate also the behavior of ellipsoidal particles." It had taken several decades to accomplish that simply stated goal [3].

Nonspherical particles are abundant in natural and artificial environments (Fig. 1). Furthermore, it has become universally recognized that nonsphericity (or more generally, complex morphology) of particles has a profound effect on their scattering and absorption properties [9]. Yet our knowledge and understanding of how nonspherical particles scatter and absorb electromagnetic energy remains incomplete and in some respects unsatisfactory.

The main goal of this tutorial review is to provide an accessible introduction to the subject of electromagnetic scattering by nonspherical particles and discuss the most general and typical ways in which the scattering and absorption properties of particles are affected by deviations of the particle morphology from that of a perfect sphere. Specifically, I will focus on

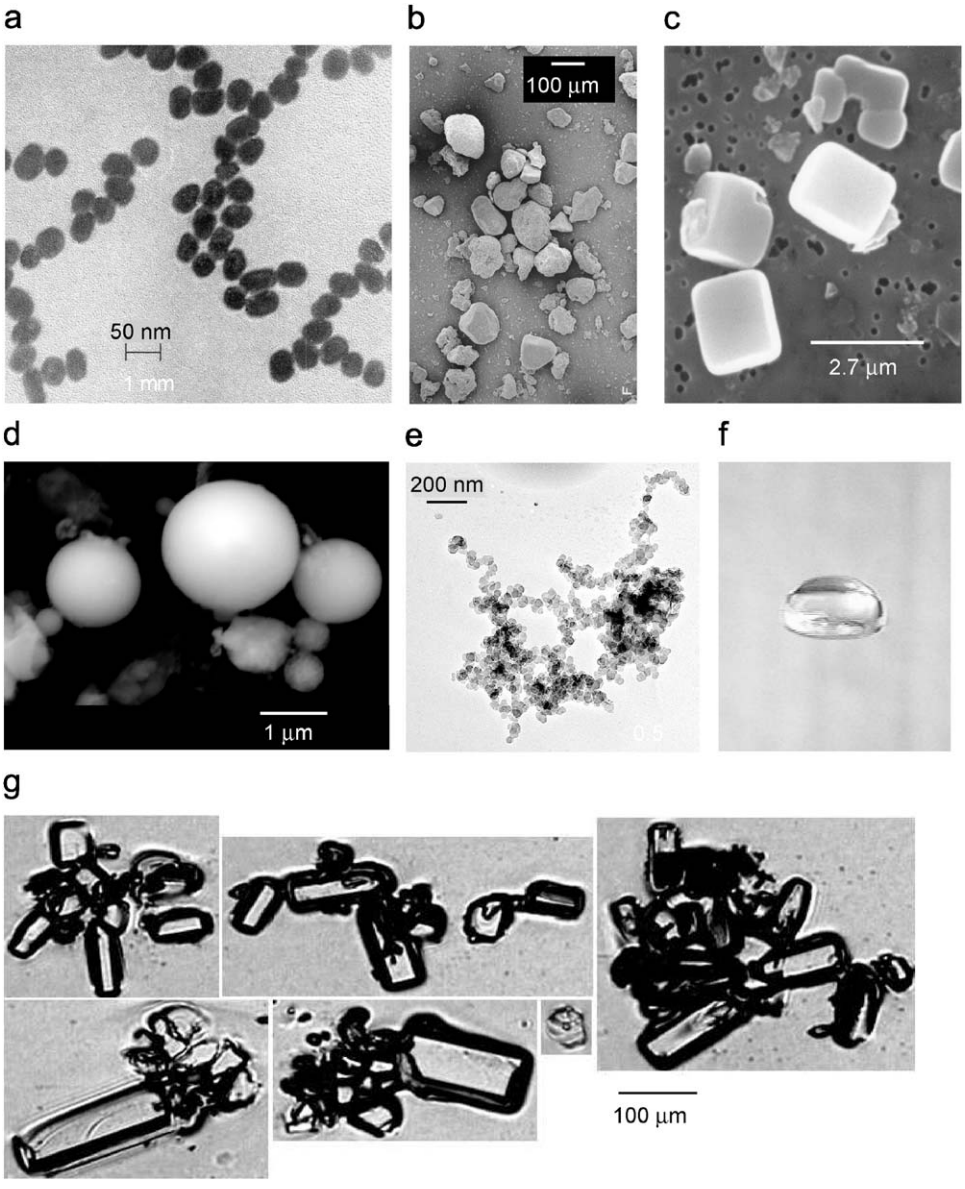

Fig. 1. Examples of man-made and natural small particles: (a) 40-nm gold particles [3], (b) Sahara desert sand particles [4], (c) dry sea-salt particles [5], (d) fly ash particles [6], (e) a soot aggregate [7], (f) a 6-mm-diameter falling raindrop, and (g) cirrus-cloud crystals [8].

how nonsphericity influences our way of describing and quantifying electromagnetic scattering by particles and how it is likely to affect, both qualitatively and quantitatively, the principal theoretical descriptors of scattering and the relevant optical observables.

Given how vast the subject of electromagnetic scattering by nonspherical particles has become, it can no longer be covered comprehensively in a review paper and even in one monograph. Therefore, this tutorial paper has several fundamental restrictions. First of all, I will not discuss specifically the commonly used theoretical and experimental techniques for the computation and measurement of electromagnetic scattering since those are well covered in the monographs [9–18] as well as in recent reviews of exact numerical methods by Kahnert [19] and Wriedt [20]. Secondly, I consider only frequency-domain scattering by assuming that all sources and fields vary in time harmonically and do not discuss transient electromagnetic phenomena [11,21], in particular the scattering of ultra-short laser pulses. Thirdly, I consider only electromagnetic scattering in the far-field zone of a particle. Near-field scattering effects are also very interesting and important, especially in connection with the rapidly developing discipline of nano-optics [22], and have become the subject of intense research. An instructive introduction to the physics of the near field is provided by [23]. Fourthly, I will focus on the effects of nonsphericity on single scattering of light by individual particles and small particle groups. In other words, manifestations of particle nonsphericity in electromagnetic scattering by large random particle groups such as clouds, particulate surfaces, and particle suspensions will not be discussed. Finally, there will be no in-depth discussion of the various applications of electromagnetic scattering by nonspherical particles in science and engineering. A plentiful source of that information is the collection of monographs [9,24–34] supplemented by several special issues of *JQSRT* published over the past years [35–49].

Essentially all quantitative illustrative examples of electromagnetic scattering given in this review are either the result of a direct measurement performed in a controlled laboratory setting or a numerically exact theoretical computation. By giving preference to exact theoretical results I do not mean to question the importance and utility of various approximate theoretical approaches: in many cases an approximate technique is the only practical way of describing electromagnetic scattering by particles. Instead, I simply follow Mie's philosophy of applying an exact theoretical approach to a somewhat idealized particle morphology rather than an approximate technique to a seemingly more realistic particle model. The virtues of this approach are rather obvious. First, a numerically exact result remains exact irrespective of what specific technique was used to obtain it and is not subject to future change or improvement besides, perhaps, infrequent attempts to re-compute it with one or two more decimals. As a consequence, the basic conclusions drawn in this review are also unlikely to change. Secondly, analyses of measurement results based on an exact theoretical technique are more definitive since they are not affected by uncertainties regarding the range of applicability and numerical accuracy of an approximate technique and/or the likely physical meaning of *ad hoc* model parameters not following directly from the Maxwell equations. Thirdly, the actual morphology of many natural and artificial particles is so complex that claims of the ability to model these morphologies "more realistically" with an approximate scattering technique are justified less often than not. This latter aspect of modeling electromagnetic scattering by ensembles of complex nonspherical particles will be discussed specifically in Section 11 in connection with the so-called statistical approach.

2. Electromagnetic scattering by a fixed particle

The gist of the fundamental concept of electromagnetic scattering by a fixed particle used in Mie's paper is explained in [2,50] and will not be discussed in much detail here. In brief, we assume that the unbounded host medium surrounding the particle is homogeneous, linear, isotropic, and nonabsorbing. The particle is illuminated by a plane electromagnetic wave given by

$$\left.\begin{aligned}\mathbf{E}^{\rm inc}(\mathbf{r},t) &= \mathbf{E}_0^{\rm inc}\exp(\mathrm{i}\mathbf{k}^{\rm inc}\cdot\mathbf{r}-\mathrm{i}\omega t)\\ \mathbf{H}^{\rm inc}(\mathbf{r},t) &= \mathbf{H}_0^{\rm inc}\exp(\mathrm{i}\mathbf{k}^{\rm inc}\cdot\mathbf{r}-\mathrm{i}\omega t)\end{aligned}\right\}\quad \mathbf{r}\in\Re^3, \tag{1}$$

with constant amplitudes $\mathbf{E}_0^{\rm inc}$ and $\mathbf{H}_0^{\rm inc}$, where $\mathbf{E}$ is the electric and $\mathbf{H}$ the magnetic field, t is time, $\mathbf{r}$ is the position (radius) vector, ω is the angular frequency, $\mathbf{k}^{\rm inc}$ is the (real-valued) wave vector, $\mathrm{i}=(-1)^{1/2}$, and $\Re^3$ denotes the entire three-dimensional space. Alternatively, it can be illuminated by a quasi-monochromatic parallel beam of light given by

$$\left.\begin{aligned}\mathbf{E}^{\rm inc}(\mathbf{r},t) &= \mathbf{E}_0^{\rm inc}(t)\exp(\mathrm{i}\mathbf{k}^{\rm inc}\cdot\mathbf{r}-\mathrm{i}\omega t)\\ \mathbf{H}^{\rm inc}(\mathbf{r},t) &= \mathbf{H}_0^{\rm inc}(t)\exp(\mathrm{i}\mathbf{k}^{\rm inc}\cdot\mathbf{r}-\mathrm{i}\omega t)\end{aligned}\right\}\quad \mathbf{r}\in\Re^3, \tag{2}$$

where fluctuations in time of the complex amplitudes of the electric and magnetic fields, $\mathbf{E}_0^{\rm inc}(t)$ and $\mathbf{H}_0^{\rm inc}(t)$, around their respective mean values occur much more slowly than the harmonic oscillations of the time factor $\exp(-\mathrm{i}\omega t)$.

These assumptions imply that all sources and fields are time harmonic and allow one to fully describe the total electromagnetic field at any moment in time everywhere in space as the solution of the frequency-domain macroscopic differential Maxwell equations [21,51]. Specifically, it is convenient to factor out the time-harmonic dependence of the electric and magnetic fields: $\mathbf{E}(\mathbf{r},t)=\exp(-\mathrm{i}\omega t)\mathbf{E}(\mathbf{r})$ and $\mathbf{H}(\mathbf{r},t)=\exp(-\mathrm{i}\omega t)\mathbf{H}(\mathbf{r})$. The electric and magnetic field amplitudes

$\mathbf{E}(\mathbf{r})$ and $\mathbf{H}(\mathbf{r})$ can then be found from the following curl equations:

$$\left.\begin{array}{l}\nabla\times\mathbf{E}(\mathbf{r})=\mathrm{i}\omega\mu_0\mathbf{H}(\mathbf{r})\\ \nabla\times\mathbf{H}(\mathbf{r})=-\mathrm{i}\omega\varepsilon_1\mathbf{E}(\mathbf{r})\end{array}\right\}\quad \mathbf{r}\in V_{\mathrm{EXT}}, \tag{3}$$

$$\left.\begin{array}{l}\nabla\times\mathbf{E}(\mathbf{r})=\mathrm{i}\omega\mu_0\mathbf{H}(\mathbf{r})\\ \nabla\times\mathbf{H}(\mathbf{r})=-\mathrm{i}\omega\varepsilon_2(\mathbf{r},\omega)\mathbf{E}(\mathbf{r})\end{array}\right\}\quad \mathbf{r}\in V_{\mathrm{INT}}. \tag{4}$$

Here V_{INT} is the cumulative "interior" volume occupied by the scattering particle; V_{EXT} is the infinite exterior region such that $V_{\mathrm{INT}}\cup V_{\mathrm{EXT}}=\Re^3$; the host medium and the scattering object are assumed to be nonmagnetic; μ_0 is the permeability of a vacuum; ε_1 is the real-valued electric permittivity of the host medium; and $\varepsilon_2(\mathbf{r},\omega)$ is the complex permittivity of the particle. Since the first relations in Eqs. (3) and (4) yield the magnetic field provided that the electric field is known everywhere, the solution of Eqs. (3) and (4) is usually sought in terms of only the electric field. In order to have a unique solution, Eqs. (3) and (4) must be supplemented by appropriate boundary conditions at the particle surface as well as by the radiation conditions at infinity [52,53].

Note that although the amplitudes $\mathbf{E}(\mathbf{r})$ and $\mathbf{H}(\mathbf{r})$ do not depend on time explicitly, they can fluctuate randomly if the incident light is quasi-monochromatic (see Eq. (2)). However, such fluctuations are assumed to occur much more slowly than the time-harmonic oscillations described by the factor $\exp(-\mathrm{i}\omega t)$, which justifies the use of the frequency-domain Maxwell equations at any given moment.

Eq. (1) represents the transport of electromagnetic energy from one point to another in the absence of the particle and embodies the concept of a perfectly monochromatic parallel beam of light. In particular, the plane electromagnetic wave propagates in an infinite nonabsorbing medium without a change in its intensity or polarization state, as shown schematically in Fig. 2a. However, the presence of the particle modifies the electromagnetic field that would exist otherwise. It is this modification that is called *electromagnetic scattering* [2,50]. It is customary to call the difference between the total field in the presence of the object (i.e., $\mathbf{E}(\mathbf{r},t)$) and the original field that would exist in the absence of the object (i.e., $\mathbf{E}^{\mathrm{inc}}(\mathbf{r},t)$) the scattered field and denote it $\mathbf{E}^{\mathrm{sca}}(\mathbf{r},t)$ (see Fig. 2b). Thus, the total field in the presence of the object is intentionally represented as the sum of the respective incident (original) and scattered fields:

$$\mathbf{E}(\mathbf{r},t)=\mathbf{E}^{\mathrm{inc}}(\mathbf{r},t)+\mathbf{E}^{\mathrm{sca}}(\mathbf{r},t). \tag{5}$$

Of course, one can think of incident fields other than a plane wave and thereby generalize the concept of scattering. In this regard, an especially convenient framework is provided by the so-called volume integral equation (VIE) which follows from the frequency-domain macroscopic Maxwell equations, is exact, and incorporates the boundary and radiation conditions [54,55]:

$$\begin{aligned}\mathbf{E}(\mathbf{r})&=\mathbf{E}^{\mathrm{inc}}(\mathbf{r})+k_1^2\int_{V_{\mathrm{INT}}}\mathrm{d}\mathbf{r}'\,\overleftrightarrow{G}(\mathbf{r},\mathbf{r}')\cdot\mathbf{E}(\mathbf{r}')[m^2(\mathbf{r}')-1]\\ &=\mathbf{E}^{\mathrm{inc}}(\mathbf{r})+k_1^2\left(\overleftrightarrow{I}+\frac{1}{k_1^2}\nabla\otimes\nabla\right)\cdot\int_{V_{\mathrm{INT}}}\mathrm{d}\mathbf{r}'\mathbf{E}(\mathbf{r}')\frac{\exp(\mathrm{i}k_1|\mathbf{r}-\mathbf{r}'|)}{4\pi|\mathbf{r}-\mathbf{r}'|}[m^2(\mathbf{r}')-1],\quad \mathbf{r}\in\Re^3,\end{aligned} \tag{6}$$

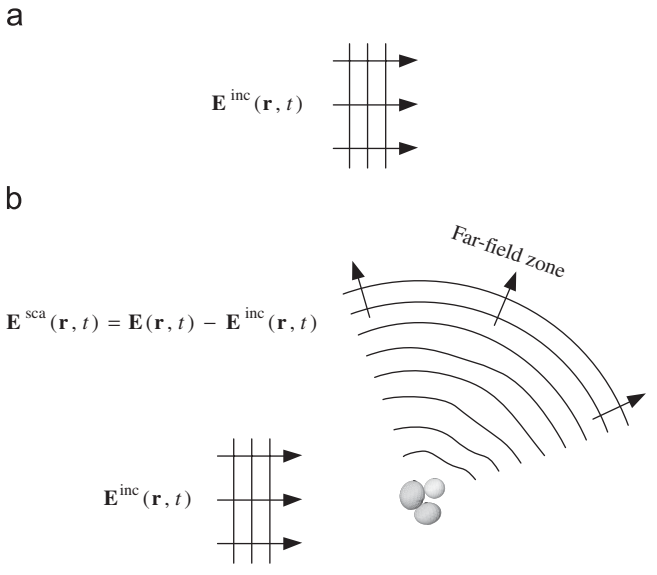

Fig. 2. Scattering by a fixed particle. In this case the particle consists of three distinct monomers in contact.

where the common factor $\exp(-i\omega t)$ is omitted, $m(\mathbf{r}') = [\varepsilon_2(\mathbf{r}', \omega)/\varepsilon_1]^{1/2}$ is the refractive index of the interior relative to that of the host exterior medium, $k_1 = |\mathbf{k}^{\rm inc}| = \omega(\varepsilon_1\mu_0)^{1/2}$ is the wave number in the host medium, $\overleftrightarrow{G}(\mathbf{r}, \mathbf{r}')$ is the free-space dyadic Green's function, $\overleftrightarrow{I}$ is the identity dyadic, and $\otimes$ is the dyadic product sign. One can see that the VIE expresses the total field everywhere in space in terms of the total internal field. The latter is not known in general and must be found by solving the VIE either analytically or numerically. It is, therefore, convenient to express the scattered electric field directly in terms of the incident field:

$$\mathbf{E}^{\rm sca}(\mathbf{r}) = \int_{V_{\rm INT}} d\mathbf{r}' \, \overleftrightarrow{G}(\mathbf{r}, \mathbf{r}') \cdot \int_{V_{\rm INT}} d\mathbf{r}'' \, \overleftrightarrow{T}(\mathbf{r}', \mathbf{r}'') \cdot \mathbf{E}^{\rm inc}(\mathbf{r}''), \quad \mathbf{r} \in \Re^3, \tag{7}$$

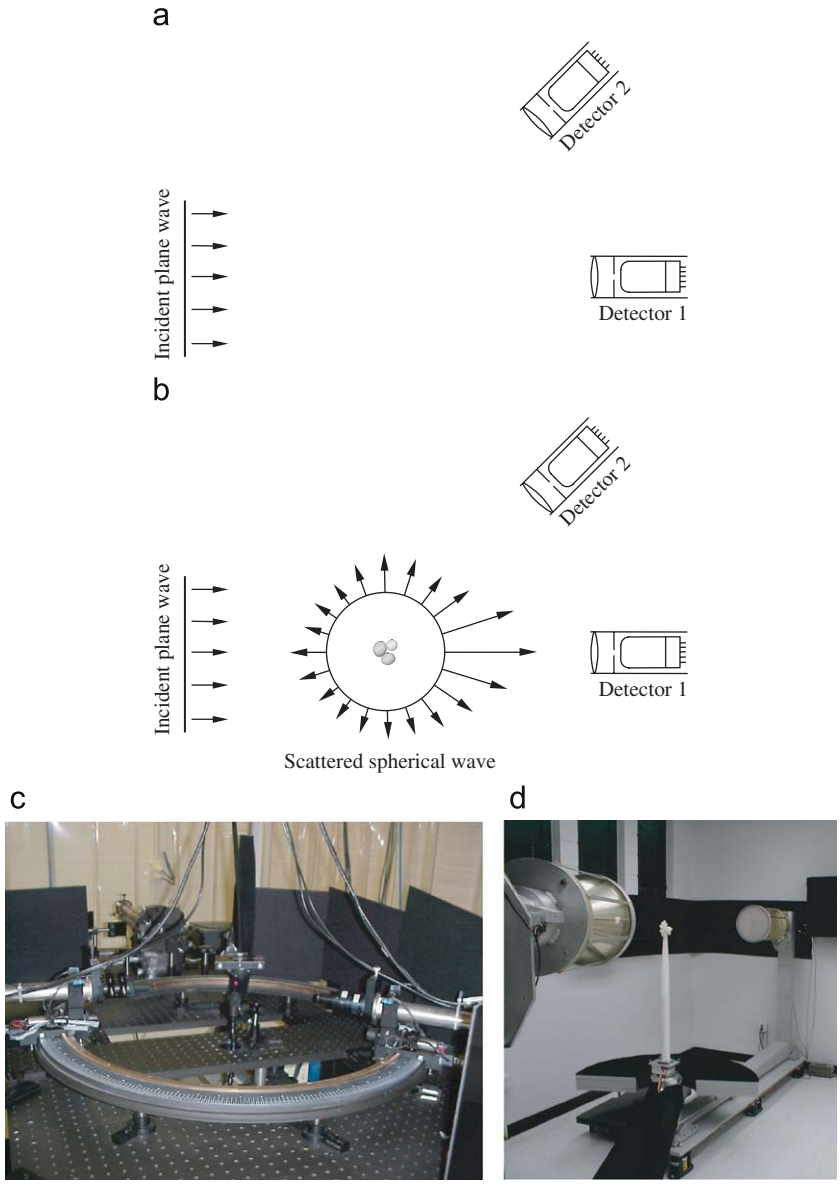

Fig. 3. (a) and (b) The readings of detectors 1 and 2 of electromagnetic energy in the presence of a particle differ from those in the absence of the particle, (c) light scattering setup built at the University of Amsterdam (http://www.astro.uva.nl/scatter). On the left is a mobile detector sliding along the ring. The detector on the right is affixed to the ring and serves as a stability monitor. In the middle of the photograph is the nozzle of the aerosol generator, and the bright red spot is where the particles exiting the nozzle cross the beam from the NeHe laser seen in the back, and (d) microwave scattering facility built at the University of Florida (http://www.astro.ufl.edu/~gustaf/facilities/LAB-ASTRO.html). The fixed scattering object in the center is illuminated by a transmitting antenna affixed to a stationary, vibration-dampened, and temperature-stabilized mount. A mobile but otherwise similarly mounted receiving antenna to the left is identical to the transmitting antenna.

where $\overleftrightarrow{T}$ is the so-called dyadic transition operator of the scattering object [56]. By substituting Eq. (7) in Eq. (6) we obtain the following equation for $\overleftrightarrow{T}$:

$$\overleftrightarrow{T}(\mathbf{r},\mathbf{r}') = k_1^2[m^2(\mathbf{r})-1]\delta(\mathbf{r}-\mathbf{r}')\,\overleftrightarrow{I} + k_1^2[m^2(\mathbf{r})-1]\int_{V_{\rm INT}} d\mathbf{r}''\,\overleftrightarrow{G}(\mathbf{r},\mathbf{r}'')\cdot\overleftrightarrow{T}(\mathbf{r}'',\mathbf{r}'), \quad \mathbf{r},\mathbf{r}'\in V_{\rm INT}, \tag{8}$$

where $\delta(\mathbf{r})$ is the three-dimensional delta function.

It has not been proven mathematically that Eq. (8) has a solution and that this solution is unique. Therefore, one has to believe in the existence and uniqueness of solution based on what is usually called "simple physical considerations". However, the indisputable advantages of Eqs. (7) and (8) are that $\overleftrightarrow{T}$ is the property of the scattering object only, is independent of the incident field, and provides a complete description of electromagnetic scattering by the object for any incident time-harmonic field.

The very nature of electromagnetic scattering makes any measurement of scattering a two-stage procedure, as illustrated in Fig. 3. First one must take the readings of detectors of electromagnetic energy in the absence of the scattering particle (Fig. 3a) and then follow up by taking the readings of the same detectors in the presence of the particle (Fig. 3b). The differences between the readings quantify the scattering and absorption properties of the particle and can be interpreted in order to infer the particle microphysical properties. Sometimes the first stage is implicit (e.g., it is often bypassed by assuming that the reading of detector 2 in the absence of the scattering object is zero), while sometimes it is dubbed "detector calibration". However, this does not change the two-stage character of any scattering measurement. Two classical implementations of this scattering measurement concept are the laboratory setups shown in Figs. 3c and d [57–60].

The ubiquitous presence of electromagnetic scattering in natural and artificial environments explains its fundamental importance in accurate modeling of electromagnetic energy transport for various science and engineering applications. The same is true of the situations in which electromagnetic scattering is induced artificially and used for particle characterization purposes in laboratory, field, and remote-sensing experiments [9,24–34]. There are several exact theoretical and numerical techniques for the computation of the scattered field. These techniques have somewhat different ranges of applicability in terms of the object morphology and object size relative to the incident wavelength and are reviewed thoroughly in [9–20].

3. Far-field scattering

An important property of the dyadic Green's function is the asymptotic behavior

$$\overleftrightarrow{G}(\mathbf{r},\mathbf{r}') \underset{r\to\infty}{\to} (\overleftrightarrow{I} - \hat{\mathbf{r}}\otimes\hat{\mathbf{r}})\frac{\exp(ik_1 r)}{4\pi r}\exp(-ik_1\hat{\mathbf{r}}\cdot\mathbf{r}'), \tag{9}$$

where $r=|\mathbf{r}|$ and $\hat{\mathbf{r}}=\mathbf{r}/r$. By placing the origin of the laboratory coordinate system O close to the geometrical center of the scattering particle, as shown in Fig. 4, and substituting Eqs. (1) and (9) in Eq. (7), we derive [15,55]

$$\mathbf{E}^{\rm sca}(\mathbf{r}) \underset{r\to\infty}{\to} \frac{\exp(ik_1 r)}{r}\mathbf{E}_1^{\rm sca}(\hat{\mathbf{n}}^{\rm sca}) = \frac{\exp(ik_1 r)}{r}\overleftrightarrow{A}(\hat{\mathbf{n}}^{\rm sca},\hat{\mathbf{n}}^{\rm inc})\cdot\mathbf{E}_0^{\rm inc}, \quad \hat{\mathbf{n}}^{\rm sca}\cdot\mathbf{E}_1^{\rm sca}(\hat{\mathbf{n}}^{\rm sca}) = 0. \tag{10}$$

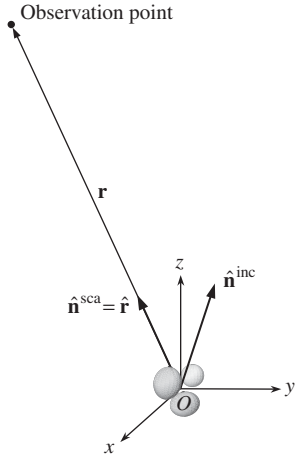

Fig. 4. Scattering in the far-field zone of the particle.

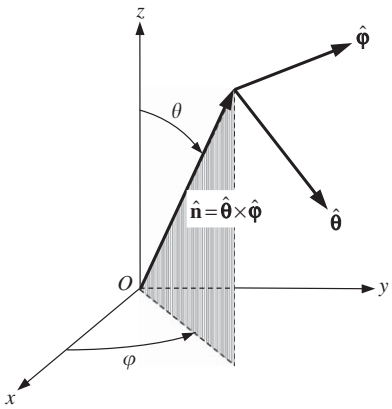

Fig. 5. Right-handed spherical coordinate system.

Here $\hat{\mathbf{n}}^{\rm inc}=\mathbf{k}^{\rm inc}/k_1$ is a unit vector in the incidence direction, $\hat{\mathbf{n}}^{\rm sca}=\hat{\mathbf{r}}$ is a unit vector in the scattering direction, and $\overleftrightarrow{A}$ is the scattering dyadic such that

$$\hat{\mathbf{n}}^{\rm sca}\cdot\overleftrightarrow{A}(\hat{\mathbf{n}}^{\rm sca},\hat{\mathbf{n}}^{\rm inc})=\overleftrightarrow{A}(\hat{\mathbf{n}}^{\rm sca},\hat{\mathbf{n}}^{\rm inc})\cdot\hat{\mathbf{n}}^{\rm inc}=\mathbf{0}, \tag{11}$$

where $\mathbf{0}$ is a zero vector. The scattering dyadic has the dimension of length. It describes the scattering of a plane electromagnetic wave in the *far-field zone* of the object where the scattered electromagnetic wave propagates away from the object, with its electric and magnetic field vectors vibrating in the plane perpendicular to the propagation direction and decaying inversely with distance from the object.

The conditions defining the far-field zone are as follows [61]:

$$k_1(r-a)\gg 1, \tag{12}$$

$$r\gg a, \tag{13}$$

$$r\gg\frac{k_1a^2}{2}, \tag{14}$$

where a is the radius of the smallest circumscribing sphere of the entire scattering particle centered at O. The principal convenience of the far-field approximation is that it allows one to treat the entire particle essentially as a point source of scattered radiation and reduces the scattered field to a simple outgoing spherical wave, as shown schematically in Fig. 2b. In addition, Eq. (11) shows that only four out of the nine components of the scattering dyadic are independent in the spherical polar coordinate system centered at the origin (see Fig. 4). It is therefore possible to introduce a 2×2 amplitude scattering matrix S expressing the θ- and φ-components of the incident plane wave in the θ- and ϕ-components of the scattered spherical wave:

$$\mathsf{E}^{\rm sca}(r\hat{\mathbf{n}}^{\rm sca})=\frac{\exp({\rm i}k_1r)}{r}\mathsf{S}(\hat{\mathbf{n}}^{\rm sca},\hat{\mathbf{n}}^{\rm inc})\mathsf{E}_0^{\rm inc}. \tag{15}$$

Here E denotes a two-element column formed by the θ- and φ-components of the electric field vector:

$$\mathsf{E}=\begin{bmatrix}E_\theta\\E_\varphi\end{bmatrix}, \tag{16}$$

$\theta\in[0,\pi]$ is the polar (zenith) angle measured from the positive z-axis and $\varphi\in[0,2\pi)$ is the azimuth angle measured from the positive x-axis in the clockwise direction when looking in the direction of the positive z-axis (see Fig. 5). The amplitude scattering matrix has the dimension of length and depends on the directions of incidence and scattering as well as on the size, morphology, and composition of the scattering object and its orientation with respect to the reference frame. It also depends on the choice of the origin of the reference frame with respect to the object.

4. Optical observables

The typically high frequency of time-harmonic electromagnetic oscillations makes it virtually impossible to measure the electric and magnetic fields associated with the incident and scattered waves using traditional optical instruments. Therefore, in order to make the theory applicable to analyses of actual optical observations, the scattering phenomenon must be characterized in terms of derivative quantities that can be measured directly (i.e., actual optical *observables*). The conventional approach to address this problem was proposed by Stokes [62]. He introduced four real-valued quantities

I, Q, U, and V which have the dimension of monochromatic energy flux ($\mathrm{W\,m^{-2}}$) and fully characterize a transverse electromagnetic wave inasmuch as it is subject to practical optical analysis. These quantities, called the Stokes parameters, are always defined with respect to a plane containing the direction of wave propagation, form the four-element Stokes column vector $\mathbf{I}$, and carry information about both the total intensity, I, and the polarization state of the wave. The Stokes parameters are intentionally defined such that the rapidly oscillating time-harmonic factor $\exp(-i\omega t)$ vanishes upon multiplication by its complex-conjugate counterpart: $\exp(-i\omega t)[\exp(-i\omega t)]^* \equiv 1$, where the asterisk denotes complex conjugation. The ellipsometric content of the Stokes parameters of monochromatic as well as quasi-monochromatic light is discussed in detail in [15,55].

In the case of far-field scattering, both the incident plane wave and the outgoing scattered spherical wave are transverse. This allows one to define the corresponding sets of Stokes parameters:

$$\mathbf{I}^{\mathrm{inc}} = \begin{bmatrix} I^{\mathrm{inc}} \\ Q^{\mathrm{inc}} \\ U^{\mathrm{inc}} \\ V^{\mathrm{inc}} \end{bmatrix} = \frac{1}{2}\sqrt{\frac{\varepsilon_1}{\mu_0}} \begin{bmatrix} E_{0\theta}^{\mathrm{inc}}(E_{0\theta}^{\mathrm{inc}})^* + E_{0\varphi}^{\mathrm{inc}}(E_{0\varphi}^{\mathrm{inc}})^* \\ E_{0\theta}^{\mathrm{inc}}(E_{0\theta}^{\mathrm{inc}})^* - E_{0\varphi}^{\mathrm{inc}}(E_{0\varphi}^{\mathrm{inc}})^* \\ -E_{0\theta}^{\mathrm{inc}}(E_{0\varphi}^{\mathrm{inc}})^* - E_{0\varphi}^{\mathrm{inc}}(E_{0\theta}^{\mathrm{inc}})^* \\ \mathrm{i}[E_{0\varphi}^{\mathrm{inc}}(E_{0\theta}^{\mathrm{inc}})^* - E_{0\theta}^{\mathrm{inc}}(E_{0\varphi}^{\mathrm{inc}})^*] \end{bmatrix}, \tag{17}$$

$$\mathbf{I}^{\mathrm{sca}}(r\hat{\mathbf{n}}^{\mathrm{sca}}) = \begin{bmatrix} I^{\mathrm{sca}} \\ Q^{\mathrm{sca}} \\ U^{\mathrm{sca}} \\ V^{\mathrm{sca}} \end{bmatrix} = \frac{1}{r^2}\frac{1}{2}\sqrt{\frac{\varepsilon_1}{\mu_0}} \begin{bmatrix} E_{1\theta}^{\mathrm{sca}}(E_{1\theta}^{\mathrm{sca}})^* + E_{1\varphi}^{\mathrm{sca}}(E_{1\varphi}^{\mathrm{sca}})^* \\ E_{1\theta}^{\mathrm{sca}}(E_{1\theta}^{\mathrm{sca}})^* - E_{1\varphi}^{\mathrm{sca}}(E_{1\varphi}^{\mathrm{sca}})^* \\ -E_{1\theta}^{\mathrm{sca}}(E_{1\varphi}^{\mathrm{sca}})^* - E_{1\phi}^{\mathrm{sca}}(E_{1\theta}^{\mathrm{sca}})^* \\ \mathrm{i}[E_{1\varphi}^{\mathrm{sca}}(E_{1\theta}^{\mathrm{sca}})^* - E_{1\theta}^{\mathrm{sca}}(E_{1\varphi}^{\mathrm{sca}})^*] \end{bmatrix}. \tag{18}$$

Then the responses of well-collimated polarization-sensitive detectors of electromagnetic energy located in the far-field zone of the particle can be described in terms of the 4×4 phase and extinction matrices as follows.

Detector 2 in Fig. 3b collects only the scattered light, and its polarized reading is fully characterized by the product of the phase matrix $\mathbf{Z}$ and the Stokes column vector of the incident wave:

$$\mathrm{Signal2} = \Delta S\mathbf{I}^{\mathrm{sca}}(r\hat{\mathbf{n}}^{\mathrm{sca}}) = \frac{\Delta S}{r^2}\mathbf{Z}(\hat{\mathbf{n}}^{\mathrm{sca}},\hat{\mathbf{n}}^{\mathrm{inc}})\mathbf{I}^{\mathrm{inc}}, \quad \hat{\mathbf{n}}^{\mathrm{sca}} \neq \hat{\mathbf{n}}^{\mathrm{inc}}, \tag{19}$$

where ΔS is the area of the sensitive surface of the detector. The elements of the phase matrix have the dimension of area and are quadratic combinations of the elements of the amplitude scattering matrix $\mathbf{S}(\hat{\mathbf{n}}^{\mathrm{sca}},\hat{\mathbf{n}}^{\mathrm{inc}})$ [15,55]. One can see that, in general, the phase matrix relates the Stokes parameters of the incident and scattered waves defined with respect to different reference planes: the meridional plane of the incidence direction $\hat{\mathbf{n}}^{\mathrm{inc}}$ and that of the scattering direction $\hat{\mathbf{n}}^{\mathrm{sca}}$, respectively. This means that the phase matrix does not represent a tensor.

Unlike detector 2, detector 1 in Fig. 3b is facing the incident light, and, accordingly, its polarized reading consists of three parts:

1. the one due to the incident light;
2. the one due to the forward-scattered light; and
3. the one due to the interference of the incident wave and the wave scattered by the object in the exact forward direction:

$$\mathrm{Signal1} = \int_{\Delta S} \mathrm{d}S\mathbf{I}(r\hat{\mathbf{r}}) = \Delta S\mathbf{I}^{\mathrm{inc}} + \frac{\Delta S}{r^2}\mathbf{Z}(\hat{\mathbf{n}}^{\mathrm{inc}},\hat{\mathbf{n}}^{\mathrm{inc}})\mathbf{I}^{\mathrm{inc}} - \mathbf{K}(\hat{\mathbf{n}}^{\mathrm{inc}})\mathbf{I}^{\mathrm{inc}} \tag{20}$$

$$\underset{r\to\infty}{=} \Delta S\mathbf{I}^{\mathrm{inc}} - \mathbf{K}(\hat{\mathbf{n}}^{\mathrm{inc}})\mathbf{I}^{\mathrm{inc}} \tag{21}$$

[15,55]. The third part is described by minus the product of the extinction matrix $\mathbf{K}$ and the Stokes column vector of the incident wave. The elements of the extinction matrix also have the dimension of area and are linear combinations of the elements of the forward-scattering amplitude matrix $\mathbf{S}(\hat{\mathbf{n}}^{\mathrm{inc}},\hat{\mathbf{n}}^{\mathrm{inc}})$.

It is worth repeating that in many respects, the measurement situation depicted in Figs. 3a and b embodies the practical meaning of the concept of electromagnetic scattering. Indeed, it demonstrates that in the absence of the particle, detector 2 would measure no signal, while the signal measured by detector 1 would be given by $\Delta S\mathbf{I}^{\mathrm{inc}}$. In the presence of the object, the readings of both detectors change. The reading of detector 2 is now proportional to the Stokes column vector of the scattered spherical wave, while the polarization signal measured by detector 1 is modified in two ways. First, the total measured electromagnetic power is attenuated as a combined result of the scattering of electromagnetic energy by the object in all directions and, possibly, the transformation of electromagnetic energy into other forms of energy (such as heat) inside the object. Second, the attenuation rates for the four Stokes components of the measured signal can, in general, be different. The latter effect is typical of objects lacking perfect spherical symmetry and is called dichroism.

Thus, to describe far-field scattering means, in effect, to quantify the differences between the readings of detectors 1 and 2 in the presence of the object and in the absence of the object. This quantification can be fully achieved in terms of the

phase and extinction matrices which depend on object characteristics such as size, shape, refractive index, and orientation. Both matrices can be readily computed provided that the amplitude scattering matrix is already known.

If the incident light is a quasi-monochromatic parallel beam then the electric field amplitude $\mathbf{E}_0^{\rm inc}$ randomly fluctuates in time. However, these fluctuations occur much more slowly than the harmonic oscillations caused by the factor $\exp(-i\omega t)$, which means that the formalism of Sections 2 and 3 remains valid at any given moment in time. Therefore, Eqs. (19)–(21) also remain valid provided that now the Stokes column vectors of the incident and scattered light are defined as averages of the right-hand sides of Eqs. (17) and (18) over a time interval much longer than the typical period of fluctuations.

It should be noted that the operational definition of the phase and extinction matrices according to Eqs. (19)–(21) [15,55] is consistent with the classical treatment in [63] and can be generalized to the case of an absorbing host medium [64–66]. Yet the practical use of the operational definition of extinction requires certain precautions [67–69].

5. Derivative quantities

There are several derivative quantities that are often used to describe various manifestations of electromagnetic scattering. The product of the extinction cross section and the intensity of the incident plane wave yields the total attenuation of the electromagnetic power measured by detector 1 in Fig. 3b owing to the presence of the particle. This means that the extinction cross section depends on the polarization state of the incident wave and is given by [15,55]

$$C_{\rm ext}(\hat{\mathbf{n}}^{\rm inc}) = \frac{1}{I^{\rm inc}}[K_{11}(\hat{\mathbf{n}}^{\rm inc})I^{\rm inc} + K_{12}(\hat{\mathbf{n}}^{\rm inc})Q^{\rm inc} + K_{13}(\hat{\mathbf{n}}^{\rm inc})U^{\rm inc} + K_{14}(\hat{\mathbf{n}}^{\rm inc})V^{\rm inc}]. \tag{22}$$

The product of the scattering cross section and the intensity of the incident plane wave yields the total far-field power scattered by the particle in all directions. We thus have [15,55]

$$\begin{aligned} C_{\rm sca}(\hat{\mathbf{n}}^{\rm inc}) &\underset{r\to\infty}{=} \frac{r^2}{I^{\rm inc}}\int_{4\pi} d\hat{\mathbf{r}} I^{\rm sca}(r\hat{\mathbf{r}}) \\ &= \frac{1}{I^{\rm inc}}\int_{4\pi} d\hat{\mathbf{r}}[Z_{11}(\hat{\mathbf{r}},\hat{\mathbf{n}}^{\rm inc})I^{\rm inc} + Z_{12}(\hat{\mathbf{r}},\hat{\mathbf{n}}^{\rm inc})Q^{\rm inc} + Z_{13}(\hat{\mathbf{r}},\hat{\mathbf{n}}^{\rm inc})U^{\rm inc} + Z_{14}(\hat{\mathbf{r}},\hat{\mathbf{n}}^{\rm inc})V^{\rm inc}], \end{aligned} \tag{23}$$

which means that $C_{\rm sca}$ also depends on the polarization state as well as on the propagation direction of the incident wave. The absorption cross section is defined as the difference between the extinction and scattering cross sections:

$$C_{\rm abs}(\hat{\mathbf{n}}^{\rm inc}) = C_{\rm ext}(\hat{\mathbf{n}}^{\rm inc}) - C_{\rm sca}(\hat{\mathbf{n}}^{\rm inc}) \geqslant 0. \tag{24}$$

All optical cross sections have the dimension of area. Finally, the dimensionless single-scattering albedo is defined as the ratio of the scattering and extinction cross sections:

$$\tilde{\omega}(\hat{\mathbf{n}}^{\rm inc}) = \frac{C_{\rm sca}(\hat{\mathbf{n}}^{\rm inc})}{C_{\rm ext}(\hat{\mathbf{n}}^{\rm inc})} \leqslant 1. \tag{25}$$

A particular case of the phase matrix is the scattering matrix defined by

$$\mathsf{F}(\Theta) = \mathsf{Z}(\theta^{\rm sca} = \Theta, \varphi^{\rm sca} = 0; \theta^{\rm inc} = 0, \varphi^{\rm inc} = 0), \quad \Theta \in [0,\pi], \tag{26}$$

where Θ, traditionally called the scattering angle, is the angle between the incidence and scattering directions. It is easy to see that the scattering matrix relates the Stokes parameters of the incident and scattered waves defined with respect to the same so-called scattering plane, i.e., the plane through the incidence and scattering directions [15,55,63,70].

6. Scattering by a "random" particle

Strictly speaking, the above formalism applies only to scattering by a fixed particle. However, one often encounters situations in which the scattering particle moves, rotates, and perhaps changes its size and/or shape during the measurement. A typical example is the measurement of scattering by a single particle suspended in air or vacuum with one of the existing levitation techniques [71]. The particle position within the levitator trap volume and its orientation are never perfectly fixed, and the particle can undergo random or periodic movements and can spin. The particle may also change its size and shape as a result of evaporation, sublimation, condensation, or melting. The shape of a liquid drop can also change owing to surface oscillations.

In this case Eqs. (19)–(21) remain valid [55] provided that (i) the distance from the trap volume to the detectors is much greater than the volume size and (ii) the particle phase, extinction, and scattering matrices entering Eqs. (19)–(21) are averaged over a sufficiently long period of time and are given by

$$\langle \mathsf{Z}(\hat{\mathbf{n}}^{\rm sca},\hat{\mathbf{n}}^{\rm inc})\rangle_t = \langle \mathsf{Z}(\hat{\mathbf{n}}^{\rm sca},\hat{\mathbf{n}}^{\rm inc})\rangle_\xi, \tag{27}$$

$$\langle \mathsf{K}(\hat{\mathbf{n}}^{\rm inc})\rangle_t = \langle \mathsf{K}(\hat{\mathbf{n}}^{\rm inc})\rangle_\xi, \tag{28}$$

$$\langle \mathsf{F}(\Theta)\rangle_t = \langle \mathsf{F}(\Theta)\rangle_\xi. \tag{29}$$

Here $\langle \dots \rangle_t$ denotes averaging over time, while $\langle \mathsf{Z}(\hat{\mathbf{n}}^{\rm sca}, \hat{\mathbf{n}}^{\rm inc}) \rangle_\xi$, $\langle \mathsf{K}(\hat{\mathbf{n}}^{\rm inc}) \rangle_\xi$, and $\langle \mathsf{F}(\Theta) \rangle_\xi$ are the phase, extinction, and scattering matrices computed with respect to the particle-centered coordinate system and averaged over all particle states ξ physically realizable during the measurement. The state of a particle indicates collectively its size, refractive index, shape, orientation, etc. i.e., all physical characteristics except the position. Obviously, the time averages of the extinction, scattering, and absorption cross sections are then given by

$$\langle C_{\rm ext}(\hat{\mathbf{n}}^{\rm inc}) \rangle_t = \langle C_{\rm ext}(\hat{\mathbf{n}}^{\rm inc}) \rangle_\xi, \tag{30}$$

$$\langle C_{\rm sca}(\hat{\mathbf{n}}^{\rm inc}) \rangle_t = \langle C_{\rm sca}(\hat{\mathbf{n}}^{\rm inc}) \rangle_\xi, \tag{31}$$

$$\langle C_{\rm abs}(\hat{\mathbf{n}}^{\rm inc}) \rangle_t = \langle C_{\rm abs}(\hat{\mathbf{n}}^{\rm inc}) \rangle_\xi, \tag{32}$$

while the single-scattering albedo is given by the ratio of the average scattering and extinction cross sections:

$$\tilde{\omega}(\hat{\mathbf{n}}^{\rm inc}) = \frac{\langle C_{\rm sca}(\hat{\mathbf{n}}^{\rm inc}) \rangle_\xi}{\langle C_{\rm ext}(\hat{\mathbf{n}}^{\rm inc}) \rangle_\xi}. \tag{33}$$

7. Scattering by a random particle group

Although we have been so far discussing electromagnetic scattering by a "single particle", the concept of electromagnetic scattering and all formulas of Section 2 remain valid irrespective of the specific morphology of the scattering object. In particular, they are valid for what a human eye could classify as a "collection of discrete particles". Examples of such "many-particle" objects are clouds, particulate surfaces, and particle suspensions. In all such cases the incident field perceives a morphologically complex "many-particle" object at any moment in time as one scatterer in the form of a specific spatial distribution of the relative refractive index [50,55].

However, the numerically exact computer solution of the Maxwell equations becomes prohibitively expensive when the size parameter of the object (i.e., the product of the wave number k_1 and the radius of the smallest circumscribing sphere of the object) exceeds $\sim$100. Furthermore, the criterion (14) makes the concept of far field inapplicable in the majority of practical situations involving large many-particle groups. For example, one often uses detectors of electromagnetic energy positioned inside the many-particle scattering object such as a cloud, in which case the concept of far field becomes completely meaningless. As a consequence, one has to resort to an approximate computational technique and often abandon the attractively simple formulas of far-field scattering.

Two conventional approaches widely used to treat electromagnetic scattering by random particle groups are the single-scattering approximation (SSA) and the combination of the radiative transfer theory (RTT) and the theory of weak localization (WL) of electromagnetic waves (otherwise known as the theory of coherent backscattering (CB)). The SSA [55,72] is applicable to a relatively small, "optically tenuous" random group of N particles viewed from a distance much greater than the entire size of the group. In this case Eqs. (19)–(21) remain valid provided that (i) the scattering signal is accumulated over a time interval long enough to average out dynamic-scattering effects and establish full ergodicity of the group [50,55,73] and (ii) the phase, extinction, and scattering matrices of the entire group are averaged over time and are given by

$$\langle Z(\hat{\mathbf{n}}^{\rm sca}, \hat{\mathbf{n}}^{\rm inc}) \rangle_t = N \langle Z_1(\hat{\mathbf{n}}^{\rm sca}, \hat{\mathbf{n}}^{\rm inc}) \rangle_\xi, \tag{34}$$

$$\langle \mathsf{K}(\hat{\mathbf{n}}^{\rm inc}) \rangle_t = N \langle \mathsf{K}_1(\hat{\mathbf{n}}^{\rm inc}) \rangle_\xi, \tag{35}$$

$$\langle \mathsf{F}(\Theta) \rangle_t = N \langle \mathsf{F}_1(\Theta) \rangle_\xi. \tag{36}$$

Here $\langle Z_1(\hat{\mathbf{n}}^{\rm sca}, \hat{\mathbf{n}}^{\rm inc}) \rangle_\xi$, $\langle \mathsf{K}_1(\hat{\mathbf{n}}^{\rm inc}) \rangle_\xi$, and $\langle \mathsf{F}_1(\Theta) \rangle_\xi$ are the single-particle phase, extinction, and scattering matrix, respectively, computed with respect to the particle-centered coordinate system and averaged over all physically realizable particle states ξ in the group. Obviously, the time averages of the extinction, scattering, and absorption cross sections of the entire random particle group can be expressed in terms of the respective ensemble-averaged single-particle cross sections:

$$\langle C_{\rm ext}(\hat{\mathbf{n}}^{\rm inc}) \rangle_t = N \langle C_{\rm ext,1}(\hat{\mathbf{n}}^{\rm inc}) \rangle_\xi, \tag{37}$$

$$\langle C_{\rm sca}(\hat{\mathbf{n}}^{\rm inc}) \rangle_t = N \langle C_{\rm sca,1}(\hat{\mathbf{n}}^{\rm inc}) \rangle_\xi, \tag{38}$$

$$\langle C_{\rm abs}(\hat{\mathbf{n}}^{\rm inc}) \rangle_t = N \langle C_{\rm abs,1}(\hat{\mathbf{n}}^{\rm inc}) \rangle_\xi. \tag{39}$$

Finally, the single-scattering albedo of the group is given by the ratio of the ensemble-averaged single-particle scattering and extinction cross sections:

$$\tilde{\omega}(\hat{\mathbf{n}}^{\rm inc}) = \frac{\langle C_{\rm sca,1}(\hat{\mathbf{n}}^{\rm inc})\rangle_\xi}{\langle C_{\rm ext,1}(\hat{\mathbf{n}}^{\rm inc})\rangle_\xi}. \tag{40}$$

The RTT is an expressly near-field theory which allows one to model the response of detectors of electromagnetic energy located inside or relatively close to a random multi-particle scattering object [50,55,74,75]. Among the conditions of applicability of the radiative transfer equation (RTE) are the asymptotic requirement $N \to \infty$, the "low-density" requirement according to which every particle must be located in the far-field zones of all the other particles, and the assumption that the scattering signal is accumulated over a time interval long enough to establish full ergodicity of the particle group [50,55]. The integro-differential form of the RTE reads

$$\hat{\mathbf{q}} \cdot \nabla \tilde{\mathrm{I}}(\mathbf{r}, \hat{\mathbf{q}}) = -n_0 \langle \mathsf{K}_1(\hat{\mathbf{q}})\rangle_\xi \tilde{\mathrm{I}}(\mathbf{r}, \hat{\mathbf{q}}) + n_0 \int_{4\pi} \mathrm{d}\hat{\mathbf{q}}' \langle \mathsf{Z}_1(\hat{\mathbf{q}}, \hat{\mathbf{q}}')\rangle_\xi \tilde{\mathrm{I}}(\mathbf{r}, \hat{\mathbf{q}}'), \tag{41}$$

where n_0 is the average particle number density, $\mathrm{d}\hat{\mathbf{q}}'$ is an elementary solid angle centered around the unit vector $\hat{\mathbf{q}}'$, and $\tilde{\mathrm{I}}(\mathbf{r}, \hat{\mathbf{q}})$ is the so-called specific Stokes column vector having the dimension of monochromatic radiance ($\mathrm{W\,m^{-2}\,sr^{-1}}$). The latter describes the radiometric and polarimetric characteristics of electromagnetic radiation propagating in the direction of the unit vector $\hat{\mathbf{q}}$ at the observation point $\mathbf{r}$. Thus the knowledge of the ensemble-averaged single-particle phase and extinction matrices is also required in order to solve the RTE. A generalized form of the RTE valid in the case of an absorbing host medium has been derived in [76–78].

The RTE does not describe specifically the effect of WL [50,55,79–85] and in particular its main manifestation in the form of a narrow intensity peak centered at the exact backscattering direction $\hat{\mathbf{n}}^{\rm sca} = -\hat{\mathbf{n}}^{\rm inc}$. Fortunately, this effect is virtually unobservable for such large rarified objects as clouds, unless the measurements are performed with a monostatic lidar or radar and the multiple-scattering contribution to the backscattered signal is significant. It is easier to observe various manifestations of WL for densely packed particulate media [82,86,87]. The rigorous general microphysical theory of WL is extremely complex [55,88–91] and is still hardly applicable to analyses of actual experimental data. However, in the case of low-density particulate media all manifestations of WL in the exact backscattering direction can be described quantitatively in terms of a solution of the RTE [92] and thus can also be traced to specific values of the ensemble-averaged single-particle phase and extinction matrices. This result ensures the applicability of the RTT to analyses of monostatic observations with, for example, lidars and radars.

8. Spherically symmetric particles

It follows from the Mie theory [1,51,63] (or its generalizations for radially inhomogeneous particles [16]) that the extinction, scattering, and absorption cross sections and the single-scattering albedo for a spherically symmetric particle are independent of the direction of propagation and polarization state of the incident light. Furthermore, the extinction matrix is diagonal and given by

$$\mathsf{K}(\hat{\mathbf{n}}^{\rm inc}) \equiv \mathsf{K} = \begin{bmatrix} C_{\rm ext} & 0 & 0 & 0 \\ 0 & C_{\rm ext} & 0 & 0 \\ 0 & 0 & C_{\rm ext} & 0 \\ 0 & 0 & 0 & C_{\rm ext} \end{bmatrix}. \tag{42}$$

The phase matrix satisfies the symmetry relations [93]

$$\begin{aligned} \mathsf{Z}(\theta^{\rm sca}, \varphi^{\rm inc}; \theta^{\rm inc}, \varphi^{\rm sca}) &= \mathsf{Z}(\theta^{\rm sca}, -\varphi^{\rm sca}; \theta^{\rm inc}, -\varphi^{\rm inc}) \\ &= \mathbf{\Lambda}_{34} \mathsf{Z}(\theta^{\rm sca}, \varphi^{\rm sca}; \theta^{\rm inc}, \varphi^{\rm inc}) \mathbf{\Lambda}_{34}, \end{aligned} \tag{43}$$

$$\mathsf{Z}(\pi - \theta^{\rm sca}, \varphi^{\rm sca}; \pi - \theta^{\rm inc}, \varphi^{\rm inc}) = \mathbf{\Lambda}_{34} \mathsf{Z}(\theta^{\rm sca}, \varphi^{\rm sca}; \theta^{\rm inc}, \varphi^{\rm inc}) \mathbf{\Lambda}_{34}, \tag{44}$$

where

$$\mathbf{\Lambda}_{34} = \begin{bmatrix} 1 & 0 & 0 & 0 \\ 0 & 1 & 0 & 0 \\ 0 & 0 & -1 & 0 \\ 0 & 0 & 0 & -1 \end{bmatrix}. \tag{45}$$

Also, it depends only on the difference between the azimuthal angles of the scattering and incidence directions rather than on their specific values:

$$\mathsf{Z}(\hat{\mathbf{n}}^{\rm sca}, \hat{\mathbf{n}}^{\rm inc}) = \mathsf{Z}(\theta^{\rm sca}, \theta^{\rm inc}, \varphi^{\rm sca} - \varphi^{\rm inc}). \tag{46}$$

Finally, the scattering matrix has a very simple block-diagonal structure with only four independent elements [63]:

$$\mathsf{F}(\Theta)=\begin{bmatrix} F_{11}(\Theta) & F_{12}(\Theta) & 0 & 0 \\ F_{12}(\Theta) & F_{11}(\Theta) & 0 & 0 \\ 0 & 0 & F_{33}(\Theta) & F_{34}(\Theta) \\ 0 & 0 & -F_{34}(\Theta) & F_{33}(\Theta) \end{bmatrix}. \tag{47}$$

In addition,

$$F_{33}(0)=F_{11}(0), \tag{48}$$

$$F_{33}(\pi)=-F_{11}(\pi), \tag{49}$$

$$F_{12}(0)=F_{12}(\pi)=0, \tag{50}$$

$$F_{34}(0)=F_{34}(\pi)=0. \tag{51}$$

The above results apply also to the phase, extinction, and scattering matrices and the optical cross sections averaged over an ensemble of spherically symmetric particles.

9. General effects of nonsphericity and orientation

The discussion in this section applies equally to a fixed nonspherical particle, a "random" nonspherical particle which is perfectly or preferentially oriented during the measurement (Section 6), and to a small random particle group in which particles are also perfectly or preferentially oriented (Section 7). Then, in general,

- the 4×4 extinction matrix K or $\langle \mathsf{K}\rangle_\xi$ does not degenerate to a direction- and polarization-independent scalar extinction cross section;
- the (ensemble-averaged) extinction, scattering, and absorption cross sections and the single-scattering albedo depend on the direction and polarization state of the incident beam;
- the scattering matrix F or $\langle \mathsf{F}\rangle_\xi$ does not have the simple block-diagonal structure of Eq. (47): all 16 elements of the scattering matrix can be nonzero and depend on the orientation of the particle(s) with respect to the scattering plane rather than only on the scattering angle;
- Eqs. (48)–(51) are not valid; and
- the phase matrix Z or $\langle \mathsf{Z}\rangle_\xi$ depends on the specific values of the azimuthal angles of the incidence and scattering directions rather than on their difference and does not obey the symmetry relations (43) and (44).

Thus any of these effects can directly indicate the presence of perfectly or preferentially oriented particles lacking perfect spherical symmetry.

Fig. 6a gives an example of the dependence of the extinction cross section on the incidence direction [94]. It depicts the results of *T*-matrix computations [15,95] of the dimensionless normalized extinction $\tilde{C}_{\rm ext}=C_{\rm ext}/(\pi r_{\rm ev}^2)$ for monodisperse prolate spheroids with a semi-axis ratio of $a/b=0.9$, where $r_{\rm ev}$ is the radius of the equal-volume sphere, b is the spheroid semi-axis along the axis of rotation, and a is the semi-axis in the perpendicular direction. $\tilde{C}_{\rm ext}$ is plotted as a function of the size parameter $x_{\rm ev}=k_1 r_{\rm ev}$ and the angle β between the spheroid axis of rotation and the incidence direction. The relative refractive index of the spheroids is fixed at 1.4, and the incident light is assumed to be unpolarized. The significant overall increase of the extinction cross section $C_{\rm ext}$ with increasing β can explained by the growing area of the spheroid geometrical projection on the plane perpendicular to the incidence direction. The numerous local maxima in the surface plot of extinction are manifestations of so-called morphology-dependent resonances (MDRs) [96] which will be discussed in more detail below.

Panels (a)–(c) of Fig. 7 illustrate the shape and orientation dependence of the ratio $-F_{12}/F_{11}$ called the degree of linear polarization for unpolarized incident light. $-F_{12}/F_{11}$ is plotted as a function of the scattering angle Θ and the surface-equivalent-sphere size parameter $x_{\rm se}=k_1 r_{\rm se}$, where $r_{\rm se}$ is the radius of the surface-equivalent sphere. These panels reveal intricate distributions of the areas of positive and negative polarization first displayed in this manner for monodisperse particles by Hansen and Travis [97]. Each complex so-called "butterfly structure" is a superposition of countless MDRs of varying shape, width, and amplitude and a component caused by the interference of the incident and scattered fields. With the exception of the region of Rayleigh scattering ($x_{\rm se}\leqslant 1$), the three panels are vastly different. In particular, the polarization patterns for the same spheroids but in two different orientations resemble each other no more than either pattern resembles that for the surface-equivalent spheres. The results shown in panel (c) obviously violate the equalities (50) and thus cannot be attributed mistakenly to spherically symmetric particles. However, the specific

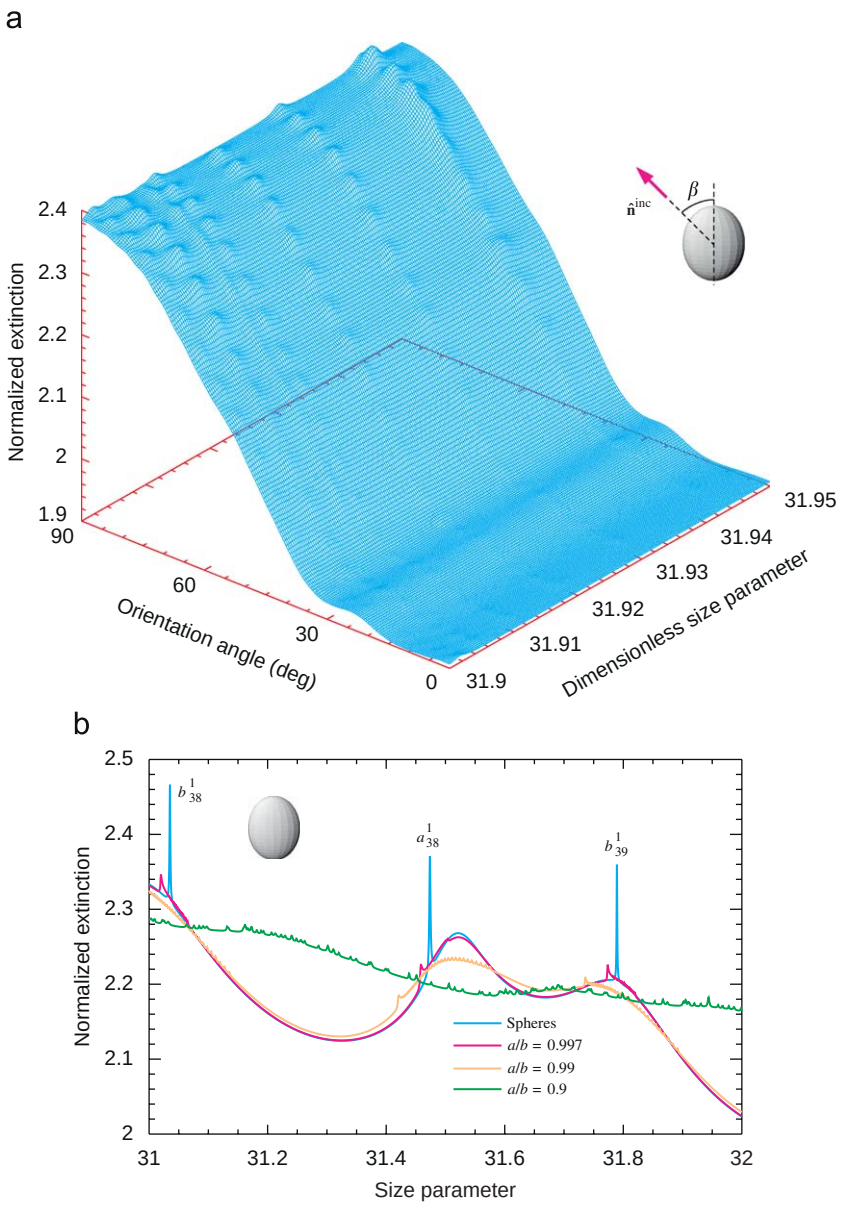

Fig. 6. (a) Normalized extinction versus volume-equivalent-sphere size parameter x_{ev} and orientation angle for monodisperse prolate spheroids with a relative refractive index of 1.4 and a semi-axis ratio of $a/b = 0.9$ and (b) normalized extinction versus volume-equivalent-sphere size parameter for monodisperse spheres and randomly oriented prolate spheroids with different semi-axis ratios a/b and a fixed relative refractive index of 1.4.

spheroid orientation used to create panel (b) does not cause a violation of Eq. (50), which shows that Eq. (50) alone cannot be used to distinguish unambiguously between a spherically symmetric particle and a nonspherical particle in a fixed orientation.

Perhaps the simplest example of preferentially oriented naturally occurring nonspherical particles are falling raindrops (Fig. 1f). The shape of these particles is axially symmetric and depends on the particle volume, becoming more oblate for larger droplets. For most remote-sensing applications the droplet shape can be approximated by that of an oblate spheroid with the shorter axis being parallel to the droplet velocity vector relative to the surrounding air mass. Therefore, the numerically accurate computation of the scattering properties of raindrops at radar wavelengths is usually straightforward and presents no difficulties [98]. The fact that the (1,2) and (2,1) elements of the scattering matrix for preferentially oriented raindrops do not vanish in the exact backscattering direction allows one to use polarization radar measurements to estimate the shape and, thus, the volume of the particles [24,98–100]. This information, coupled with the measurement of the total backscattered intensity, can be used to retrieve remotely such an important meteorological parameter as the rainfall rate.

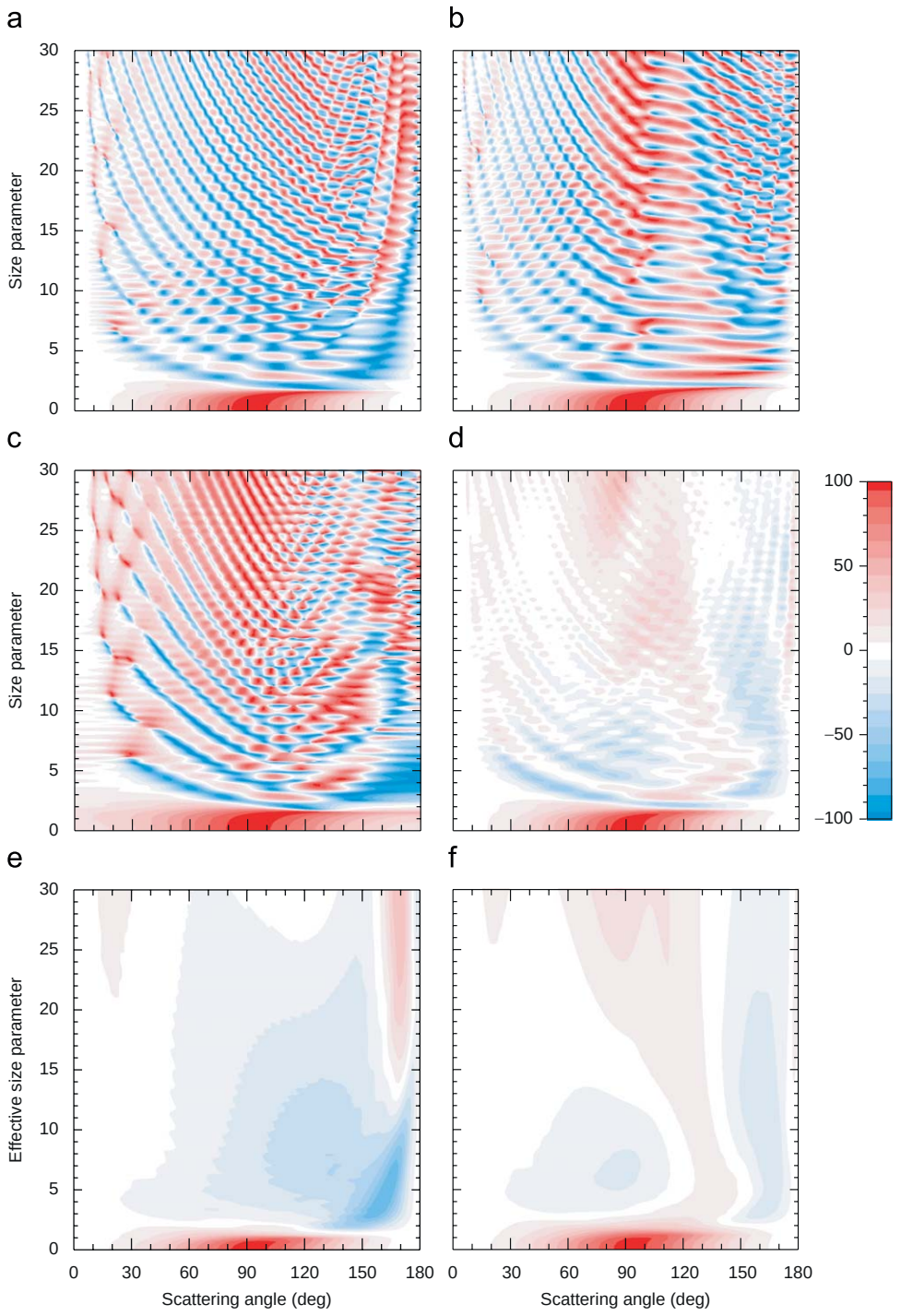

Fig. 7. (a)–(c) $-F_{12}/F_{11}$ (in %) versus Θ and x_{se} for monodisperse spheres and surface-equivalent oblate spheroids in a fixed orientation. The rotation axis of the spheroids is oriented along the incidence direction (panel b) or perpendicularly to the scattering plane (panel c), (d) $-\langle F_{12}\rangle_\xi/\langle F_{11}\rangle_\xi$ versus Θ and x_{se} for monodisperse, randomly oriented oblate spheroids, and (e)–(f) $-\langle F_{12}\rangle_\xi/\langle F_{11}\rangle_\xi$ versus Θ and effective surface-equivalent-sphere size parameter for polydisperse spheres and polydisperse, randomly oriented oblate spheroids. The relative refractive index of all particles is fixed at 1.53+i0.008 and the spheroid semi-axis ratio is fixed at $a/b = 1.7$.

10. Mirror-symmetric ensembles of randomly oriented particles: general traits

Consider now a random particle or a small random group of particles such that the distribution of particle orientations during the measurement is uniform. Furthermore, we assume that the single random particle is mirror-symmetric (i.e., has

a plane of symmetry), while each particle in the group has a plane of symmetry and/or is accompanied by its mirror counterpart. Then most of the results of Section 8 apply [15,63]. Specifically, the ensemble-averaged extinction, scattering, and absorption cross sections and the single-scattering albedo are independent of the direction of propagation and polarization state of the incident light. The ensemble-averaged extinction matrix is diagonal

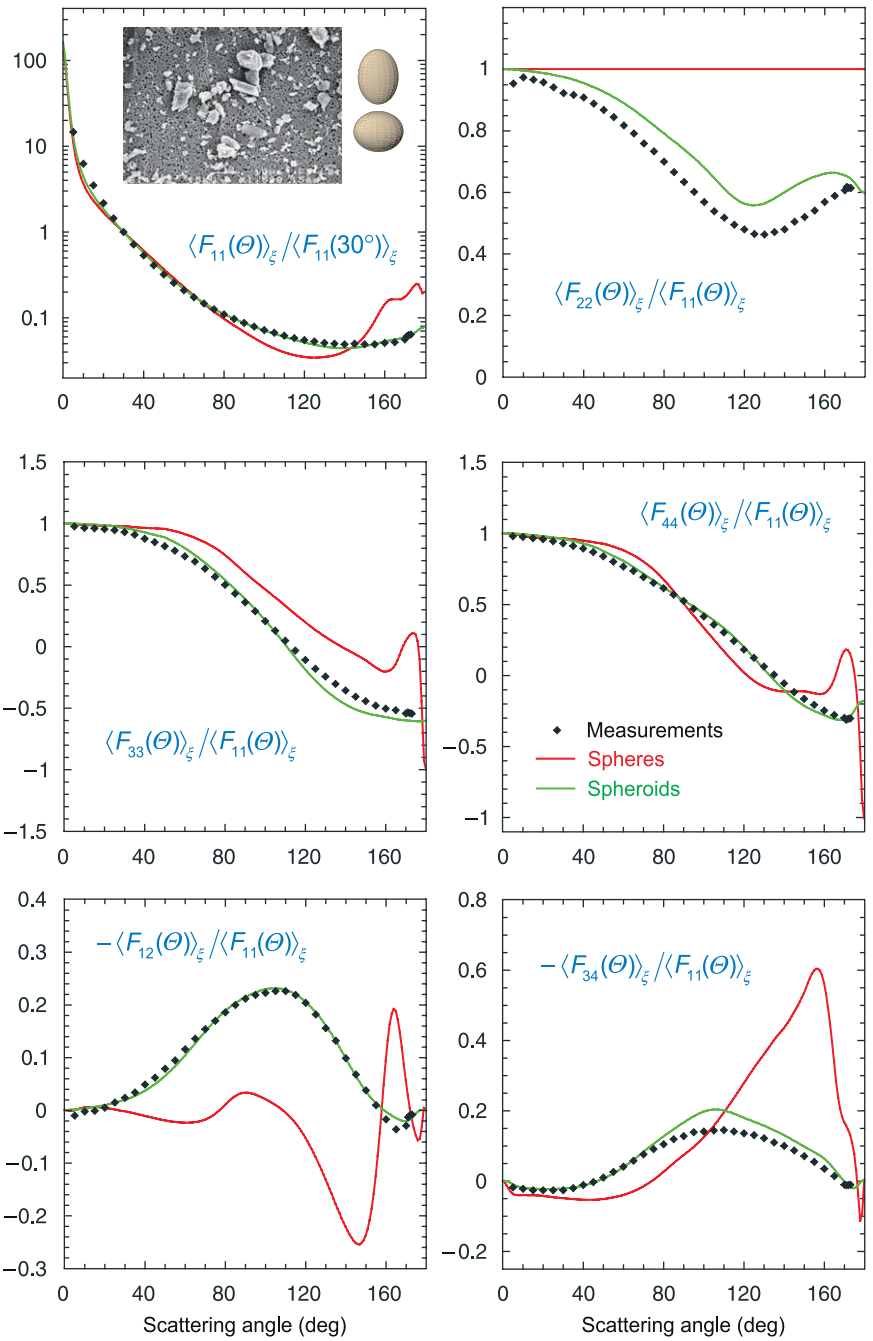

Fig. 8. Diamonds depict the results of laboratory measurements of the ensemble-averaged scattering matrix for micrometer-sized feldspar particles at a wavelength of 633 nm [4]. The green curves show the result of fitting the laboratory data with *T*-matrix results computed for a shape distribution of polydisperse, randomly oriented prolate and oblate spheroids [101]. The real and model particle shapes are contrasted in the inset. The red curves show the results of Mie computations for volume-equivalent polydisperse spherical particles. (For interpretation of the references to color in this figure legend, the reader is referred to the web version of this article.)

and given by

$$\langle \mathsf{K}(\hat{\mathbf{n}}^{\rm inc})\rangle_\xi \equiv \langle \mathsf{K}\rangle_\xi = \begin{bmatrix} \langle C_{\rm ext}\rangle_\xi & 0 & 0 & 0 \\ 0 & \langle C_{\rm ext}\rangle_\xi & 0 & 0 \\ 0 & 0 & \langle C_{\rm ext}\rangle_\xi & 0 \\ 0 & 0 & 0 & \langle C_{\rm ext}\rangle_\xi \end{bmatrix}. \tag{52}$$

The ensemble-averaged phase matrix satisfies the symmetry relations

$$\begin{aligned} \langle \mathsf{Z}(\theta^{\rm sca},\varphi^{\rm inc};\theta^{\rm inc},\varphi^{\rm sca})\rangle_\xi &= \langle \mathsf{Z}(\theta^{\rm sca},-\varphi^{\rm sca};\theta^{\rm inc},-\varphi^{\rm inc})\rangle_\xi \\ &= \mathbf{\Delta}_{34}\langle \mathsf{Z}(\theta^{\rm sca},\varphi^{\rm sca};\theta^{\rm inc},\varphi^{\rm inc})\rangle_\xi \mathbf{\Delta}_{34}, \end{aligned} \tag{53}$$

$$\langle \mathsf{Z}(\pi-\theta^{\rm sca},\varphi^{\rm sca};\pi-\theta^{\rm inc},\varphi^{\rm inc})\rangle_\xi = \mathbf{\Delta}_{34}\langle \mathsf{Z}(\theta^{\rm sca},\varphi^{\rm sca};\theta^{\rm inc},\varphi^{\rm inc})\rangle_\xi \mathbf{\Delta}_{34}, \tag{54}$$

and depends only on the difference between the azimuthal angles of the scattering and incidence directions rather than on their specific values:

$$\langle \mathsf{Z}(\hat{\mathbf{n}}^{\rm sca},\hat{\mathbf{n}}^{\rm inc})\rangle_\xi = \langle \mathsf{Z}(\theta^{\rm sca},\theta^{\rm inc},\varphi^{\rm sca}-\varphi^{\rm inc})\rangle_\xi. \tag{55}$$

The ensemble-averaged scattering matrix has a similar block-diagonal structure, but now has six rather than four independent elements:

$$\langle \mathsf{F}(\Theta)\rangle_\xi = \begin{bmatrix} \langle F_{11}(\Theta)\rangle_\xi & \langle F_{12}(\Theta)\rangle_\xi & 0 & 0 \\ \langle F_{12}(\Theta)\rangle_\xi & \langle F_{22}(\Theta)\rangle_\xi & 0 & 0 \\ 0 & 0 & \langle F_{33}(\Theta)\rangle_\xi & \langle F_{34}(\Theta)\rangle_\xi \\ 0 & 0 & -\langle F_{34}(\Theta)\rangle_\xi & \langle F_{44}(\Theta)\rangle_\xi \end{bmatrix}. \tag{56}$$

The equalities (48) and (49) are no longer valid, but the properties (50) and (51) are preserved:

$$\langle F_{12}(0)\rangle_\xi = \langle F_{12}(\pi)\rangle_\xi = 0, \tag{57}$$

$$\langle F_{34}(0)\rangle_\xi = \langle F_{34}(\pi)\rangle_\xi = 0. \tag{58}$$

The equalities (57) are illustrated by the *T*-matrix results for randomly oriented monodisperse spheroids shown in Fig. 7d.

Despite the similarity of the matrices (47) and (56), the identities $\langle F_{22}(\Theta)\rangle_\xi \equiv \langle F_{11}(\Theta)\rangle_\xi$ and $\langle F_{44}(\Theta)\rangle_\xi \equiv \langle F_{33}(\Theta)\rangle_\xi$ do not hold in general, which is well illustrated by the results of laboratory measurements for natural feldspar particles shown in Fig. 8. As a consequence, measurements of the linear backscattering depolarization ratio

$$\delta_{\rm L} = \frac{\langle F_{11}(\pi)\rangle_\xi - \langle F_{22}(\pi)\rangle_\xi}{\langle F_{11}(\pi)\rangle_\xi + \langle F_{22}(\pi)\rangle_\xi}, \quad 0 \leqslant \delta_{\rm L} \leqslant 1, \tag{59}$$

and the closely related circular backscattering depolarization ratio [102]

$$\delta_{\rm C} = \frac{\langle F_{11}(\pi)\rangle_\xi + \langle F_{44}(\pi)\rangle_\xi}{\langle F_{11}(\pi)\rangle_\xi - \langle F_{44}(\pi)\rangle_\xi} = \frac{2\delta_{\rm L}}{1-\delta_{\rm L}} \geqslant \delta_{\rm L}, \tag{60}$$

are among the most reliable means of detecting particle nonsphericity.

11. Mirror-symmetric ensembles of randomly oriented particles: quantitative traits

Of course, besides the qualitative distinctions discussed in the preceding section, there can be significant quantitative differences in specific scattering properties of randomly oriented nonspherical particles and "equivalent" (e.g., volume-equivalent or surface-equivalent) spheres. We begin by discussing the effects of nonsphericity and random orientation on MDRs. Fig. 6b summarizes the results of numerically exact *T*-matrix computations for monodisperse spheres and volume-equivalent, randomly oriented spheroids with a relative refractive index of 1.4 in the range of size parameters affected by three super-narrow Mie MDRs b_{38}^1, a_{38}^1, and b_{39}^1 as well as three broader resonance features [94]. We follow the notation introduced in [103] which implies, for example, that b_{38}^1 is the first resonance generated by the b_{38} partial Mie coefficient as the sphere size parameter increases from zero. Now the direction-independent normalized extinction is defined as the ratio $\tilde{C}_{\rm ext} = \langle C_{\rm ext}\rangle_\xi/(\pi r_{\rm ev}^2)$, where $\langle C_{\rm ext}\rangle_\xi$ is the orientation-averaged extinction cross section. It is seen that increasing the aspect ratio of the spheroids ε (the ratio of the largest to the smallest particle dimensions) rapidly reduces the height of the normalized extinction peaks. It is in fact remarkable that the deformation of a sphere by as little as one hundredth of a wavelength essentially annihilates the super-narrow MDRs. A secondary effect of increasing asphericity is to shift the resonances to smaller size parameters. Obviously, it takes significantly larger asphericities to suppress the broader MDRs. An interesting feature of the curve for $a/b = 0.9$ is the minute high-frequency ripple superposed on a slowly and weakly varying background. This ripple is absent in the curves for the nearly spherical spheroids and is the contribution of

additional natural frequencies of oscillation of distinctly aspherical spheroids with specific orientations relative to the incident beam. This effect is well seen in Fig. 6a.

The smoothing effect of averaging over orientations of a nonspherical particle on MDRs is also well seen from the comparison of Figs. 7b–d. Averaging over sizes reinforces this effect. This is demonstrated by Figs. 7e and f which parallel Figs. 7a and d, respectively, and show the ratio $-\langle F_{12}(\Theta)\rangle_\xi/\langle F_{11}(\Theta)\rangle_\xi$ computed for a modified power law size distribution of spheres and randomly oriented surface-equivalent spheroids [104]. The resulting polarization patterns are now smooth enough to derive conclusions regarding the likely quantitative effects of nonsphericity of natural polydisperse particles. Among such effects are the bridge of positive polarization at side-scattering angles and a negative polarization branch at backscattering angles measured previously for narrow size distributions of nearly cubically shaped NaCl particles with mean size parameters ranging from 3.1 to 19.9 [105] as well as for many other types of mineral particles [4,58,106].

Due to the unique properties of the super-narrow MDRs, the measurement and analysis of their various manifestations turn out to be the most accurate means for the detection of even minute deviations of the particle shape from sphericity as well as for the determination of the size and refractive index of a perfectly (or nearly perfectly) spherical particle [94,96,107–111]. The fact that even miniscule amounts of nonsphericity effectively extinguish the super-narrow MDRs is likely to simplify numerical computations for polydisperse particle ensembles such as natural cloud droplets. Indeed, it has been hypothesized that not fully resolving the MDRs owing to the use of a numerical size-integration quadrature formula with insufficiently narrow separations between the quadrature nodes may result in significant errors in broadband absorption computations [112]. The analysis in [112] was based on the assumption that cloud droplets are perfect spheres and support even the most narrow MDRs, thereby seemingly necessitating the use of quadrature formulas with extreme numbers of closely spaced quadrature nods and making computer calculations very time-consuming. However, real cloud droplets hardly have a perfectly spherical shape given many ambient factors that are likely to cause significant distortions of the droplet shape and thereby suppress the super-narrow MDRs.

We have already mentioned that backscattering depolarization measurements are widely used for detecting and characterizing nonspherical particles [113]. *T*-matrix results depicted in Fig. 9a [114] demonstrate indeed that wavelength-sized particles can produce large depolarization ratios. An interesting trait of essentially all the curves shown in this figure is a rapid increase in δ_L as the effective size parameter increases from 0 to about 10. Moreover, maximal δ_L values for most shapes are observed at size parameters close to and sometimes slightly smaller than 10. Unfortunately, the *T*-matrix results show no obvious relationship between δ_L and the particle aspect ratio. Even spheroids with aspect ratios as small as 1.05 (a 2.5% deviation from the perfect spherical shape) produce strong depolarization. In fact, the largest δ_L values are generated by prolate spheroids with aspect ratios as small as 1.2 (a 10% deviation from a sphere). Furthermore, δ_L for spheroids and, especially, cylinders tends to saturate with increasing aspect ratio. These results suggest that although a nonzero δ_L value is an unequivocal indication of particle nonsphericity it is not necessarily a measure of the degree of deviation of the particle shape from that of a perfect sphere.

Fig. 9b illustrates the use of laboratory measurements of the linear depolarization ratio as a particle characterization tool [116]. The blue symbols show the results of measurements performed at the Aerosol Interactions and Dynamics in the Atmosphere (AIDA) facility of the Forschungszentrum Karlsruhe [117,118] at the laser wavelength 488 nm. This AIDA ice cloud experiment was started at an initial temperature of 192 K and in ice saturated conditions. Nano-sized meteoric smoke analog particles were used as ice seeds. Expansion cooling of the chamber gas was initiated at $t=0$ and resulted in a gradual increase of the ice saturation ratio. After the ice supersaturation ratio was increased to about 35% (at $t=500$ s) ice crystals started to nucleate heterogeneously on the surfaces of the aerosol particles, as indicated by the steep increase of the measured depolarization ratio. The expansion cooling lasted until $t=2000$ s resulting in the growth of the ice crystals to a median equal-volume diameter of about 3 μm. The time-dependent ice crystal size distribution was retrieved from simultaneous infrared extinction measurements using theoretical computations based on the *T*-matrix method [15]. After the expansion cooling was stopped the ice cloud started to evaporate due to the heat flux from the warmer chamber walls. The best theoretical fit to the measured infrared extinction spectra was achieved by assuming oblate ice cylinders with a diameter-to-length ratio of 1.25. The use of this aspect ratio and the retrieved temporal evolution of the size distribution in subsequent *T*-matrix calculations of the linear depolarization ratio resulted in a close quantitative agreement with the corresponding laboratory data, as Fig. 9b beautifully demonstrates. Other instructive examples of such closure studies are described in [118].

Despite the significant progress in our ability to model scattering by nonspherical particles, accurate theoretical computations for many types of natural and artificial particles with sizes comparable to and greater than the wavelength (Fig. 1) remain highly problematic. Therefore, there have been several attempts to simulate the scattering and absorption properties of actual particles using simple model shapes. These attempts have been based on the realization that in addition to size and orientation averaging as discussed above, averaging over shapes may also prove to be necessary in many cases. Indeed, quite often ensembles of natural and artificial particle exhibit a vast variety of shapes, which makes questionable the utility of a single model shape (however "irregular" it may look to the human eye) in the representation of scattering properties of an ensemble.

To illustrate this point, Fig. 10a shows the phase functions, defined as

$$p(\Theta)=\frac{4\pi\langle F_{11}(\Theta)\rangle_\xi}{\langle C_{sca}\rangle_\xi}, \tag{61}$$

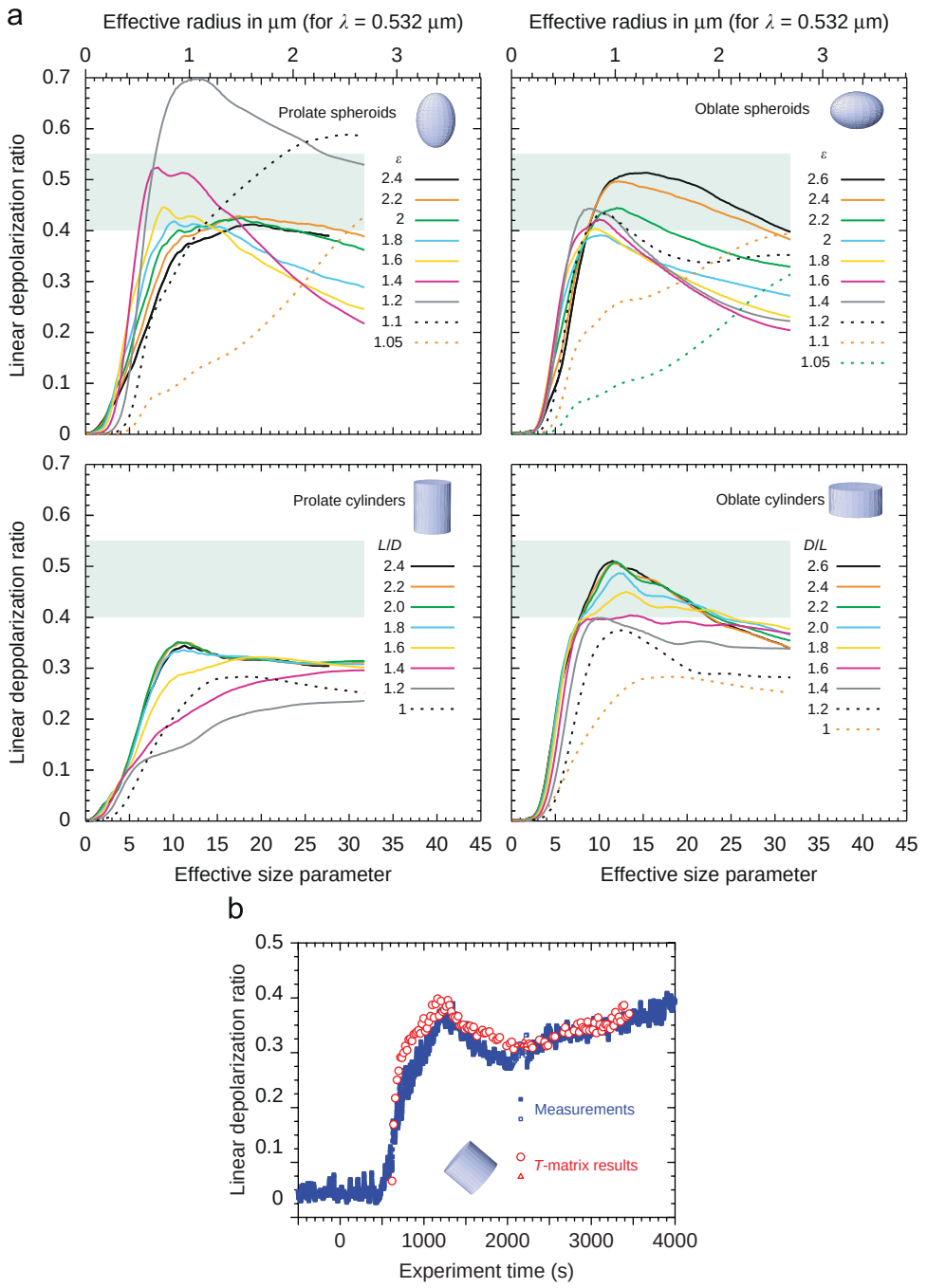

Fig. 9. (a) Linear depolarization ratio versus effective surface-equivalent-sphere size parameter for polydisperse, randomly oriented ice spheroids with aspect ratios ranging from 1.05 to 2.6 and circular cylinders with various length-to-diameter or diameter-to-length ratios. The relative refractive index is 1.311. The light-green bands show the range of highest depolarization ratios typically observed for anthropogenic cirrus clouds in the form of aircraft condensation trails [115]. The upper horizontal axes convert effective size parameters to effective radii assuming the wavelength $\lambda = 2\pi/k_1 = 0.532\,\mu m$ and (b) fit of theoretical computations to the results of laboratory measurements of the linear depolarization ratio (courtesy of Martin Schnaiter [116]). (For interpretation of the references to color in this figure legend, the reader is referred to the web version of this article.)

computed for polydisperse, randomly oriented prolate spheroids with varying aspect ratios [119]. It demonstrates indeed that even after size and orientation averaging, each spheroidal shape produces a unique, shape-specific scattering pattern, whereas laboratory and *in situ* measurements for real nonspherical particles usually show smooth, rather featureless patterns. However, the green curves in Fig. 8 show that shape mixtures of polydisperse, randomly oriented prolate and

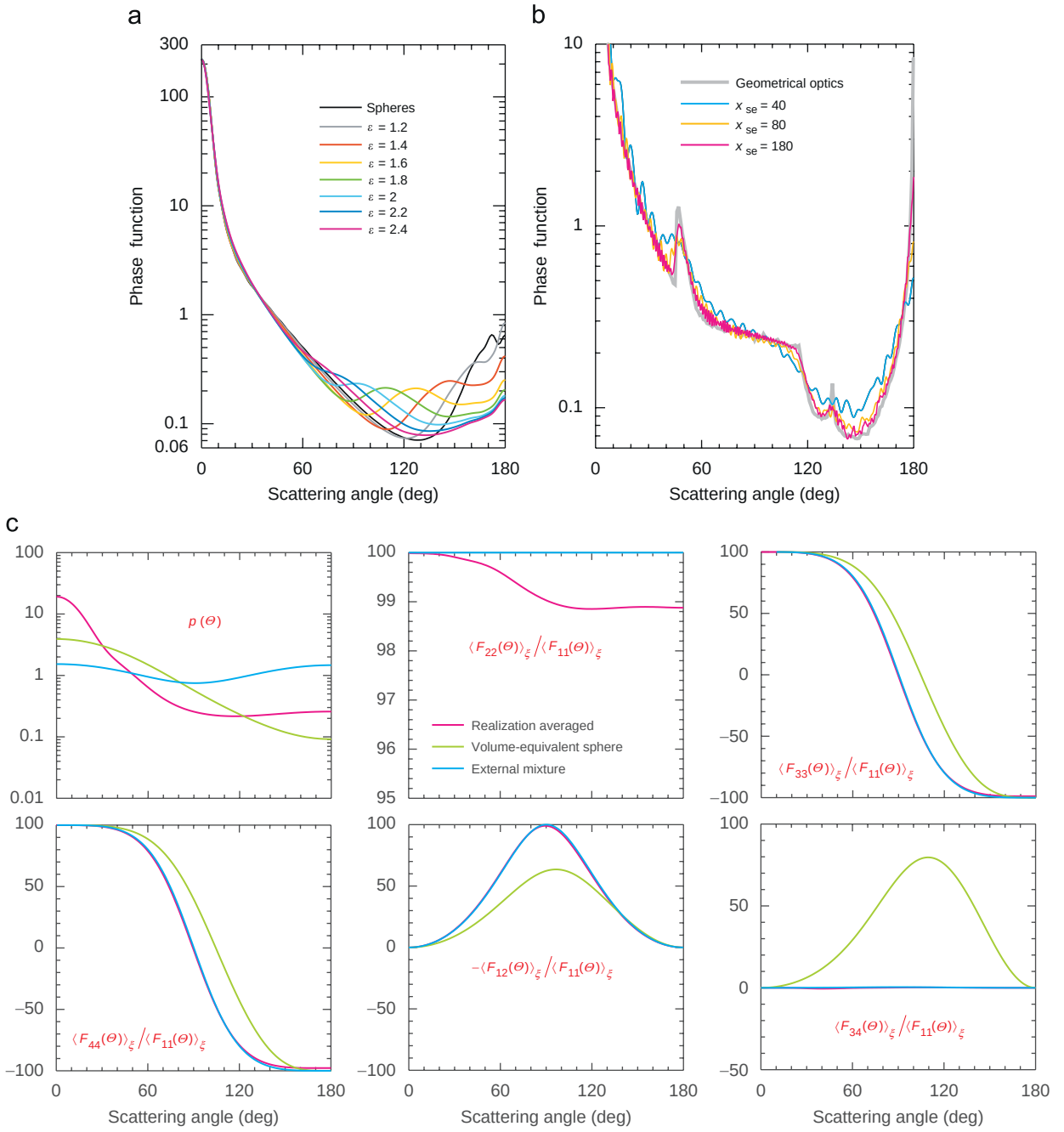

Fig. 10. (a) *T*-matrix computations of the phase function for micrometer-sized polydisperse spheres and randomly oriented surface-equivalent prolate spheroids with aspect ratios ranging from 1.2 to 2.4 at a wavelength of 443 nm. The relative refractive index is fixed at 1.53+i0.008, (b) geometric-optics and *T*-matrix phase functions for monodisperse, randomly oriented circular cylinders with surface-equivalent-sphere size parameters $x_{se} = 40$, 80, and 180. The relative refractive index is $1.311+i0.311 \times 10^{-8}$ and is typical of water ice at visible wavelengths, (c) realization-averaged scattering matrix elements for randomly oriented fractal clusters with $D_f = 1.82$, $k_0 = 1.19$, $N_S = 400$, and $a = 0.02\,\mu m$. The soot refractive index is 1.75+i0.435 and the wavelength of the incident light is 628 nm. Also shown are the results for the corresponding homogeneous volume-equivalent sphere and the "equivalent" external mixture of soot monomers. The scattering-matrix element ratios are given in percent.

oblate spheroids can provide a good quantitative fit to the results of accurate laboratory measurements of the scattering matrix for natural irregular particles.

This example leads to two important conclusions. First of all, it provides evidence that the often observed smooth scattering-angle dependence of the elements of the scattering matrix for natural and artificial ensembles of nonspherical

particles is largely caused by the diversity of particle shapes in the ensemble. Secondly, it suggests that at least some scattering properties of ensembles of irregular particles can be adequately modeled using polydisperse shape mixtures of simple particles such as spheroids. These two conclusions form the gist of the so-called statistical approach according to which particles chosen for the purpose of ensemble averaging need not be in one-to-one morphological correspondence with the actual particle ensemble and may have relatively simple shapes [119,120]. Needless to say, forming representative mixtures of less regular particles then spheroids should be expected to eventually provide an even better model of electromagnetic scattering by many natural and artificial particle ensembles (e.g., [121,122]).

Contrasting the green and the corresponding red curves in Fig. 8 provides a good illustration of the typical nonspherical–spherical differences in the elements of the scattering matrix discussed in detail in [15]. For example, several theoretical and laboratory analyses of the phase-function patterns for volume- or surface-equivalent spherical and nonspherical particles have revealed the following five distinct scattering-angle ranges:

$$\begin{aligned}
&\text{nonsphere} \approx \text{sphere} \quad \text{from } \Theta = 0^\circ \text{ to } \Theta \sim 15^\circ - 20^\circ;\\
&\text{nonsphere} > \text{sphere} \quad \text{from } \Theta \sim 15^\circ - 20^\circ \text{ to } \Theta \sim 35^\circ;\\
&\text{nonsphere} < \text{sphere} \quad \text{from } \Theta \sim 35^\circ \text{ to } \Theta \sim 85^\circ;\\
&\text{nonsphere} \gg \text{sphere} \quad \text{from } \Theta \sim 85^\circ \text{ to } \Theta \sim 150^\circ; \text{ and}\\
&\text{nonsphere} \ll \text{sphere} \quad \text{from } \Theta \sim 150^\circ \text{ to } \Theta = 180^\circ.
\end{aligned} \tag{62}$$

Although the specific boundaries of these regions can shift with particle shape and relative refractive index (e.g., [15,123]), the enhanced side-scattering and suppressed backscattering appear to be rather universal characteristics of nonspherical particles.

The degree of linear polarization for unpolarized incident light, $-\langle F_{12}(\Theta)\rangle_\xi / \langle F_{11}(\Theta)\rangle_\xi$, tends to be positive at scattering angles around 100°–120° for nonspherical particles. Whereas $\langle F_{22}(\Theta)\rangle_\xi / \langle F_{11}(\Theta)\rangle_\xi \equiv 1$ for spherically symmetric scatterers, the same ratio for nonspherical particles deviates significantly from the value 1 and exhibits strong backscattering depolarization. Similarly, $\langle F_{33}(\Theta)\rangle_\xi / \langle F_{11}(\Theta)\rangle_\xi \equiv \langle F_{44}(\Theta)\rangle_\xi / \langle F_{11}(\Theta)\rangle_\xi$ for spherically symmetric particles, whereas the ratio $\langle F_{44}(\Theta)\rangle_\xi / \langle F_{11}(\Theta)\rangle_\xi$ for nonspherical particles tends to be greater than the ratio $\langle F_{33}(\Theta)\rangle_\xi / \langle F_{11}(\Theta)\rangle_\xi$ at most scattering angles, especially in the backscattering direction. The ratios $\langle F_{34}(\Theta)\rangle_\xi / \langle F_{11}(\Theta)\rangle_\xi$ for spherical and nonspherical particles also reveal significant quantitative differences, especially at large scattering angles.

Unlike ensembles of irregularly shaped particles, regular nonspherical shapes may cause pronounced angular features in the elements of the scattering matrix, especially as the particle size starts to exceed the wavelength of the incident light. This is well illustrated by Fig. 10b which shows the results of exact T-matrix computations of the phase function for randomly oriented compact circular cylinders with surface-equivalent-sphere size parameters ranging from 40 to 180 [124]. As the size parameter increases, the T-matrix phase functions develop such typical geometric-optics features as the 46° halo and the strong and narrow backscattering peak seen in the grey curve. Such pronounced phase-function features caused by regular ice-crystal shapes are responsible for many spectacular atmospheric-optics displays [125] and affect the results of cirrus-cloud remote sensing [126–130]. In many cases, however, various imperfections of the ice-crystal shape and/or multiple internal inclusions (e.g., in the form of air bubbles) destroy sharp geometric-optics features such as halos and cause smooth and featureless phase functions similar to that depicted by diamonds in Fig. 8 [131–133].

In most cases nonspherical–spherical differences in the optical cross sections and the single-scattering albedo are not nearly as significant as those in the scattering matrix elements. The same is true of the asymmetry parameter defined as

$$g = \frac{1}{2}\int_0^\pi \mathrm{d}\Theta \, \sin\Theta p(\Theta) \cos\Theta. \tag{63}$$

This does not mean, however, that the effects of nonsphericity on the integral scattering and absorption characteristics are always negligible or unimportant [134,135]. A good example of particles characterized by integral radiometric properties vastly different from those of volume-equivalent spheres are clusters composed of large numbers of small monomers such as soot aggregates [136–139] (see Fig. 1e). Detailed computations for fractal soot clusters based on the discrete dipole approximation [140,141] and the superposition T-matrix method [142] have been reported in [143–146]. The overall morphology of a dry soot aerosol is usually described by the following statistical scaling law [139,147]:

$$N_S = k_0 \left(\frac{R_g}{a}\right)^{D_f}, \tag{64}$$

where a is the monomer mean radius, k_0 the prefactor, D_f the fractal dimension, N_S the number of spherical monomers in the cluster, and R_g, called the radius of gyration, is a measure of the overall cluster radius. The fractal dimension is especially important for the quantitative characterization of the aggregate morphology. Densely packed aggregates have D_f values close to 3, whereas the fractal dimension of chain-like branched clusters can be significantly smaller. The other important structural coefficient, k_0, is also related to the state of compactness of a fractal aggregate. Examples of computer-generated fractal clusters are given in Fig. 11. Obviously, the aggregates become more compact as D_f increases.

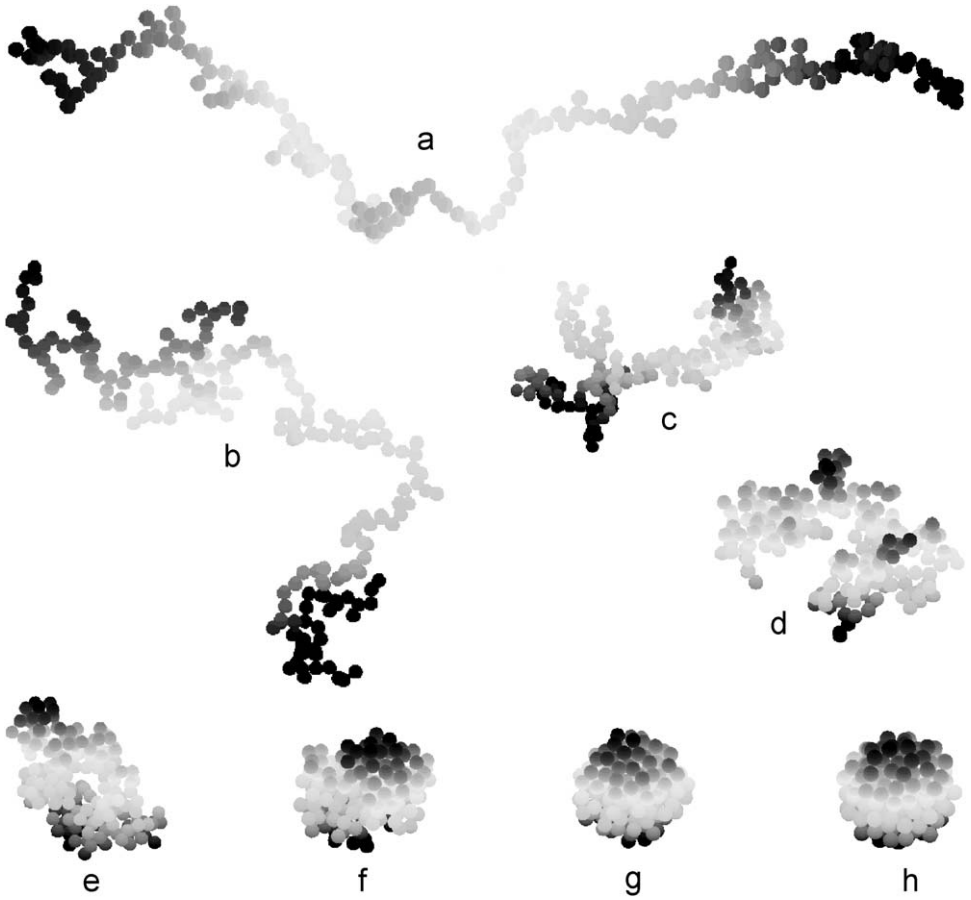

Fig. 11. Fractal aggregates composed of 200 monomers and characterized by different values of the fractal parameters D_f and k_0: (a)–(g) $D_f = 1.25$, 1.5, 1.75, 2, 2.25, 2.5, 2.75 and $k_0 = 1.6$ and (h) $D_f = 3$ and $k_0 = 1.2$.

Fig. 12 depicts the ratios of $\langle C_{ext}\rangle_\xi$, $\langle C_{sca}\rangle_\xi$, $\langle C_{abs}\rangle_\xi$, $\tilde{\omega}$, and g computed, at a wavelength of 870 nm, for randomly oriented fractal aggregates with refractive indices 1.75+i0.5 and 2+i, monomer radii 15 and 25 nm, and numbers of monomers 200, 400, 600, and 800 to those for the corresponding volume-equivalent homogeneous spheres [146]. These numerically exact T-matrix results demonstrate indeed that the integral radiometric properties of the clusters can often be profoundly different from those of the volume-equivalent spheres. This is especially true of the scattering cross section, single-scattering albedo, and asymmetry parameter.

Fig. 10c depicts the results of T-matrix computations of the scattering matrix elements averaged over 20 soot-cluster realizations randomly computer-generated for the same values of the fractal parameters [145]. In a rather peculiar way, the angular scattering properties of the soot clusters appear to be a mix of those of wavelength-sized compact particles (the nearly isotropic Rayleigh phase function of the small individual spherules evolves into a forward scattering phase function) and Rayleigh scatterers (i.e., the degree of linear polarization of scattered light for unpolarized incident light, $-\langle F_{12}(\Theta)\rangle_\xi/\langle F_{11}(\Theta)\rangle_\xi$, is zero at the exact forward- and back-scattering directions and reaches a nearly 100% maximum at $\Theta \approx 90^\circ$ [148] while the ratio $\langle F_{34}(\Theta)\rangle_\xi/\langle F_{11}(\Theta)\rangle_\xi$ is very close to zero). The deviation of the ratio $\langle F_{22}(\Theta)\rangle_\xi/\langle F_{11}(\Theta)\rangle_\xi$ from unity is the only obvious manifestation of the overall nonsphericity of the soot clusters.

Also shown for comparison in Fig. 10c are two sets of approximate results. The first set includes the results obtained by applying the SSA to the corresponding external mixture of the constituent monomers (i.e., by assuming that all monomers are widely separated and randomly positioned rather than form a cluster with touching components). The second set of results was computed by applying the Mie theory to a homogeneous sphere with a volume equal to the combined volume of the cluster monomers. Clearly, the external-mixture model provides a poor representation of the cluster phase function, whereas the performance of the equal-volume-sphere model is inadequate with respect to all scattering matrix elements.

12. Conclusions

There is no doubt that since the publication of Mie's seminal paper, our knowledge of electromagnetic scattering by nonspherical particles has improved profoundly. In particular, the general effects of nonsphericity are largely understood,

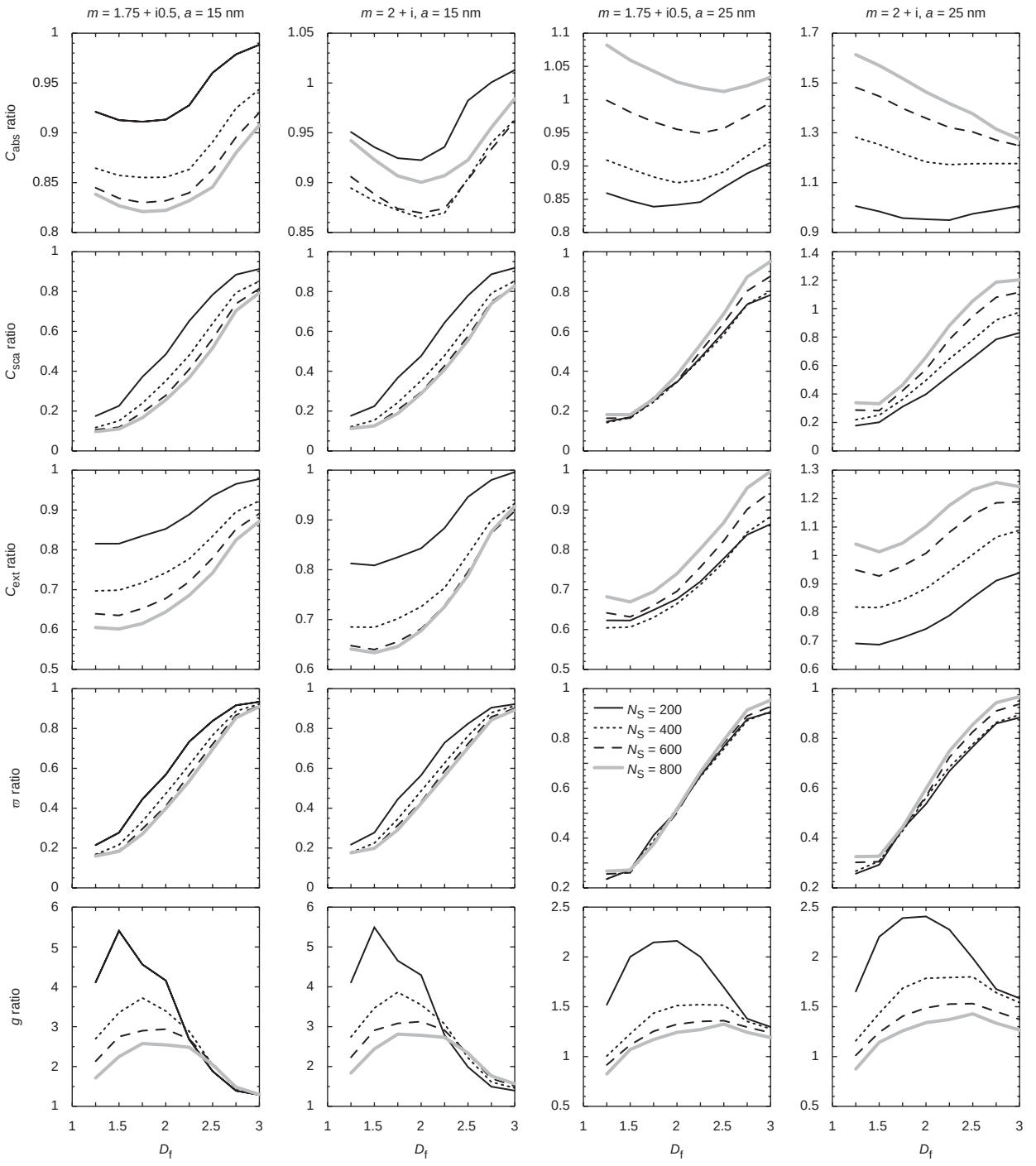

Fig. 12. Ratios of the integral optical characteristics of soot fractals to those computed for the respective volume-equivalent spheres. The wavelength of the incident light is fixed at 870 nm.

both qualitatively and quantitatively, and a vast body of practical applications have been documented. Still much remains to be done since in some respects our knowledge of specific manifestations of particle shape and morphology in electromagnetic scattering remains fragmentary and/or inadequate. However, our collective progress in this direction has been impetuous, as was convincingly demonstrated at the recent conference on "Light Scattering: Mie and More" (Karlsruhe, July 2009) [149] and the XI Conference on Electromagnetic and Light Scattering by Nonspherical Particles (Hatfield, UK, September 2009) [150]. These impressive developments allow us to look into the future with great optimism.

Acknowledgments

I thank Pat Arnott, Matthew Berg, Brian Cairns, Jacek Chowdhary, Oleg Dubovik, Joop Hovenier, Michael Kahnert, Li Liu, Daniel Mackowski, Pinar Mengüç, Martin Schnaiter, Larry Travis, Gorden Videen, Warren Wiscombe, Thomas Wriedt, and Ping Yang for numerous fruitful discussions. Martin Schnaiter has kindly contributed Fig. 9b. This research was sponsored by the NASA Radiation Sciences Program managed by Hal Maring and by the NASA Glory Mission project.

References

[1] Mie G. Beiträge zur Optik trüber Medien, speziell kolloidaler Metallösungen. Ann Physik 1908;25:377–445.
[2] Mishchenko MI, Travis LD. Gustav Mie and the evolving discipline of electromagnetic scattering by particles. Bull Am Meteorol Soc 2008;89:1853–61.
[3] Khlebtsov NG, Bogatyrev VA, Dykman LA, Melnikov AG. Spectral extinction of colloidal gold and its biospecific conjugates. J Colloid Interface Sci 1996;180:436–45.
[4] Volten H, Muñoz O, Rol E, de Haan J, Vassen W, Hovenier J, et al. Scattering matrices of mineral aerosol particles at 441.6 and 632.8 nm. J Geophys Res 2001;106:17375–402.
[5] Chamaillard K, Jennings SG, Kleefeld C, Ceburnis D, Yoon YJ. Light backscattering and scattering by nonspherical sea-salt aerosols. JQSRT 2003;79/80:577–97.
[6] Ebert M, Weinbruch S, Rausch A, Gorzawski G, Helas G, Hoffmann P, et al. Complex refractive index of aerosols during LACE 98 as derived from the analysis of individual particles. J Geophys Res 2002;107:8121.
[7] Li J, Anderson JR, Buseck PR. TEM study of aerosol particles from clean and polluted marine boundary layers over the North Atlantic. J Geophys Res 2003;108:4189.
[8] Arnott WP, Dong YY, Hallett J, Poellot MR. Role of small ice crystals in radiative properties of cirrus: a case study, FIRE II, November 22, 1991. J Geophys Res 1994;99:1371–81.
[9] Mishchenko MI, Hovenier JW, Travis LD, editors. Light scattering by nonspherical particles: theory, measurements, and applications. San Diego: Academic Press; 2000.
[10] Wriedt T, editor. Generalized multipole techniques for electromagnetic and light scattering. Amsterdam: Elsevier; 1999.
[11] Taflove A, Hagness SC. Computational electrodynamics: the finite-difference time-domain method. Boston: Artech House; 2000.
[12] Doicu A, Eremin YuA, Wriedt T. Acoustic and electromagnetic scattering analysis using discrete sources. San Diego: Academic Press; 2000.
[13] Li L-W, Kang X-K, Leong M-S. Spheroidal wave functions in electromagnetic theory. New York: Wiley; 2002.
[14] Jin J. The finite element method in electromagnetics. New York: Wiley; 2002.
[15] Mishchenko MI, Travis LD, Lacis AA. Scattering, absorption, and emission of light by small particles. Cambridge, UK: Cambridge University Press; 2002 〈http://www.giss.nasa.gov/~crmim/books.html〉.
[16] Babenko VA, Astafyeva LG, Kuzmin VN. Electromagnetic scattering in disperse media: inhomogeneous and anisotropic particles. Chichester, UK: Praxis; 2003.
[17] Doicu A, Wriedt T, Eremin YuA. Light scattering by systems of particles. Null-field method with discrete sources: theory and programs. Berlin: Springer; 2006.
[18] Borghese F, Denti P, Saija R. Scattering from model nonspherical particles. Theory and applications to environmental physics. Berlin: Springer; 2007.
[19] Kahnert FM. Numerical methods in electromagnetic scattering theory. JQSRT 2003;79–80:775–824.
[20] Wriedt T. Light scattering theories and computer codes. JQSRT 2009;110 [this issue].
[21] Van Bladel J. Electromagnetic fields. Piscataway, NJ: IEEE Press; 2007.
[22] Novotny L, Hecht B. Principles of nano-optics. Cambridge, UK: Cambridge University Press; 2006.
[23] Girard C, Joachim C, Gauthier S. The physics of the near-field. Rep Progr Phys 2000;63:893–938.
[24] Stephens GL. Remote sensing of the lower atmosphere. New York: Oxford University Press; 1994.
[25] Dolginov AZ, Gnedin YuN, Silant'ev NA. Propagation and polarization of radiation in cosmic media. Basel: Gordon and Breach; 1995.
[26] Videen G, Kocifaj M, editors. Optics of cosmic dust. Dordrecht, The Netherlands: Kluwer Academic Publishers; 2002.
[27] Liou KN. An introduction to atmospheric radiation. San Diego: Academic Press; 2002.
[28] Videen G, Yatskiv YS, Mishchenko MI, editors. Photopolarimetry in remote sensing. Dordrecht, The Netherlands: Kluwer Academic Publishers; 2004.
[29] Mätzler C, editor. Thermal microwave radiation: applications for remote sensing. London: IET Press; 2006.
[30] Kokhanovsky AA, editor. Light scattering reviews. Chichester, UK: Praxis; 2006.
[31] Kokhanovsky AA, editor. Light scattering reviews 2. Chichester, UK: Praxis; 2007.
[32] Hoekstra A, Maltsev V, Videen G, editors. Optics of biological particles. Dordrecht, The Netherlands: Springer; 2007.
[33] Jonasz M, Fournier GR. Light scattering by particles in water. Amsterdam: Elsevier; 2007.
[34] Kokhanovsky AA, editor. Light scattering reviews 3. Chichester, UK: Praxis; 2008.
[35] Hovenier JW, editor. Light scattering by non-spherical particles. JQSRT 1996;55:535–694.
[36] Lumme K, editor. Light scattering by non-spherical particles. JQSRT 1998;60:301–500.
[37] Mishchenko MI, Hovenier JW, Travis LD, editors. Light scattering by nonspherical particles'98. JQSRT 1999;63:127–738.
[38] Videen G, Fu Q, Chýlek P, editors. Light scattering by non-spherical particles. JQSRT 2001;70:373–831.
[39] Mengüç MP, Selçuk N, Howell JR, Sacadura J-F, editors. Third international symposium on radiative transfer. JQSRT 2002;73:129–528.
[40] Kolokolova L, Gustafson BÅS, Mishchenko MI, Videen G, editors. Electromagnetic and light scattering by nonspherical particles 2002. JQSRT 2003;79–80:491–1198.
[41] Videen G, Yatskiv YS, Mishchenko MI, editors. Photopolarimetry in remote sensing. JQSRT 2004;88:1–406.
[42] Wriedt T, editor. VII electromagnetic and light scattering by non-spherical particles: theory, measurement and applications. JQSRT 2004;89:1–460.
[43] Mengüç MP, Selçuk N, Webb BW, Lemonnier D, editors. Fourth international symposium on radiative transfer. JQSRT 2005;93:1–395.
[44] Moreno F, Muñoz O, López-Moreno JJ, Molina A, editors. VIII conference on electromagnetic and light scattering by nonspherical particles. JQSRT 2006;100:1–495.
[45] Stam DM, Mishchenko MI, editors. Light in planetary atmospheres and other particulate media. JQSRT 2006;101:381–556.
[46] Hoekstra A, Maltsev V, Videen G, editors. Optics of biological particles. JQSRT 2006;102:1–128.
[47] Voshchinnikov NV, Videen G, editors. IX conference on electromagnetic and light scattering by non-spherical particles. JQSRT 2007;106:1–621.
[48] Mengüç MP, Selçuk N, Webb BW, Lemonnier D, editors. The fifth international symposium on radiative transfer. JQSRT 2008;109:177–361.
[49] Mishchenko MI, Videen G, Mengüç MP, editors. X conference on electromagnetic and light scattering by non-spherical particles. JQSRT 2008;109:1335–548.
[50] Mishchenko MI. Multiple scattering, radiative transfer, and weak localization in discrete random media: unified microphysical approach. Rev Geophys 2008;46:RG2003.
[51] Stratton JA. Electromagnetic theory. New York: McGraw-Hill; 1941.
[52] Silver S, editor. Microwave antenna theory and design. New York: McGraw-Hill; 1949.

[53] Müller C. Foundations of the mathematical theory of electromagnetic waves. Berlin: Springer; 1969.
[54] Saxon DS. Lectures on the scattering of light. Scientific Report No. 9, Department of Meteorology. Los Angerel: University of California at Los Angeles; 1955.
[55] Mishchenko MI, Travis LD, Lacis AA. Multiple scattering of light by particles: radiative transfer and coherent backscattering. Cambridge, UK: Cambridge University Press; 2006.
[56] Tsang L, Kong JA, Shin RT. Theory of microwave remote sensing. New York: Wiley; 1985.
[57] Volten H, Muñoz O, Hovenier JW, Waters LBFM. An update of the Amsterdam light scattering database. JQSRT 2006;100:437–43.
[58] Muñoz O, Volten H. Experimental light scattering matrices from the Amsterdam light scattering database. Light Scattering Rev 2006;1:3–29.
[59] Gustafson BÅS. Microwave analog to light scattering measurements: a modern implementation of a proven method to achieve precise control. JQSRT 1996;55:663–72.
[60] Gustafson BÅS. Microwave analog to light-scattering measurements. In: Mishchenko MI, Hovenier JW, Travis LD, editors. Light scattering by nonspherical particles: theory, measurements, and applications. San Diego: Academic Press; 2000. p. 367–90.
[61] Mishchenko MI. Far-field approximation in electromagnetic scattering. JQSRT 2006;100:268–76.
[62] Stokes GG. On the composition and resolution of streams of polarized light from different sources. Trans Cambridge Philos Soc 1852;9:399–416.
[63] van de Hulst HC. Light scattering by small particles. New York: Dover; 1981.
[64] Bohren CF, Gilra DP. Extinction by a spherical particle in an absorbing medium. J Colloid Interface Sci 1979;72:215–21.
[65] Videen G, Sun W. Yet another look at light scattering from particles in absorbing media. Appl Opt 2003;42:6724–7.
[66] Mishchenko MI. Electromagnetic scattering by a fixed finite object embedded in an absorbing medium. Opt Express 2007;15:13188–202.
[67] Berg MJ, Sorensen CM, Chakrabarti A. Extinction and the optical theorem. I. Single particles. J Opt Soc Am A 2008;25:1504–13.
[68] Berg MJ, Sorensen CM, Chakrabarti A. Extinction and the optical theorem. II. Multiple particles. J Opt Soc Am A 2008;25:1514–20.
[69] Mishchenko M.I., Berg M.J., Sorensen C.M., van der Mee C.V.M., On definition and measurement of extinction cross section. JQSRT 2009;110:doi:10.1016/j.jqsrt.2008.11.010.
[70] Hovenier JW, Van der Mee C, Domke H. Transfer of polarized light in planetary atmospheres—basic concepts and practical methods. Dordrecht, The Netherlands: Kluwer Academic Publishers; 2004.
[71] Davis EJ, Schweiger G. The airborne microparticle: its physics, chemistry, optics, and transport phenomena. Berlin: Springer; 2002.
[72] Mishchenko MI, Liu L, Videen G. Conditions of applicability of the single-scattering approximation. Opt Express 2007;15:7522–7.
[73] Berne BJ, Pecora R. Dynamic light scattering. New York: Wiley; 1976.
[74] Mishchenko MI. Vector radiative transfer equation for arbitrarily shaped and arbitrarily oriented particles: a microphysical derivation from statistical electromagnetics. Appl Opt 2002;41:7114–34.
[75] Mishchenko MI. Microphysical approach to polarized radiative transfer: extension to the case of an external observation point. Appl Opt 2003;42:4963–7.
[76] Durant S, Calvo-Perez O, Vukadinovic N, Greffet J-J. Light scattering by a random distribution of particles embedded in absorbing media: diagrammatic expansion of the extinction coefficient. J Opt Soc Am A 2007;24:2943–52.
[77] Mishchenko MI. Multiple scattering by particles embedded in an absorbing medium. 1. Foldy–Lax equations, order-of-scattering expansion, and coherent field. Opt Express 2008;16:2288–301.
[78] Mishchenko MI. Multiple scattering by particles embedded in an absorbing medium. 2. Radiative transfer equation. JQSRT 2008;109:2386–90.
[79] Barabanenkov YuN, Kravtsov YuA, Ozrin VD, Saichev AI. Enhanced backscattering in optics. Progr Opt 1991;29:65–197.
[80] Kuz'min VL, Romanov VP. Coherent phenomena in light scattering from disordered systems. Phys—Uspekhi 1996;39:231–60.
[81] van Rossum MCW, Nieuwenhuizen ThM. Multiple scattering of classical waves: microscopy, mesoscopy, and diffusion. Rev Mod Phys 1999;71:313–71.
[82] Lenke R, Maret G. Multiple scattering of light: coherent backscattering and transmission. In: Brown W, Mortensen K, editors. Scattering in polymeric and colloidal systems. Amsterdam: Gordon and Breach; 2000. p. 1–73.
[83] van Tiggelen BA, Skipetrov SE, editors. Wave scattering in complex media: from theory to applications. Dordrecht, The Netherlands: Kluwer Academic Publishers; 2003.
[84] Sheng P. Introduction to wave scattering, localization, and mesoscopic phenomena. Berlin: Springer; 2006.
[85] Akkermans E, Montambaux G. Mesoscopic physics of electrons and photons. Cambridge, UK: Cambridge University Press; 2007.
[86] Psarev V, Ovcharenko A, Shkuratov Yu, Belskaya I, Videen G. Photometry of particulate surfaces at extremely small phase angles. JQSRT 2007;106:455–63.
[87] Gross P, et al. A precise method to determine the angular distribution of backscattered light to high angles. Rev Sci Instr 2007;78:033105.
[88] Tishkovets VP. Multiple scattering of light by a layer of discrete random medium: backscattering. JQSRT 2002;72:123–37.
[89] Tishkovets VP, Mishchenko MI. Coherent backscattering of light by a layer of discrete random medium. JQSRT 2004;86:161–80.
[90] Tishkovets VP. Incoherent and coherent backscattering of light by a layer of densely packed random medium. JQSRT 2007;108:454–63.
[91] Kobayashi S, Oguchi T, Tanelli S, Im E. Backscattering enhancement on spheroid-shaped hydrometeors: considerations in water and ice particles of uniform size and Marshall–Palmer distributed rains. Radio Sci 2007;42:RS2001.
[92] Mishchenko MI. Enhanced backscattering of polarized light from discrete random media: calculations in exactly the backscattering direction. J Opt Soc Am A 1992;9:978–82.
[93] Hovenier JW. Symmetry relationships for scattering of polarized light in a slab of randomly oriented particles. J Atmos Sci 1969;26:488–99.
[94] Mishchenko MI, Lacis AA. Morphology-dependent resonances of nearly spherical particles in random orientation. Appl Opt 2003;42:5551–6.
[95] Waterman PC. Symmetry, unitarity, and geometry in electromagnetic scattering. Phys Rev D 1971;3:825–39.
[96] Hill SC, Benner RE. Morphology-dependent resonances. In: Barber PW, Chang RK, editors. Optical effects associated with small particles. Singapore: World Scientific; 1988. p. 3–61.
[97] Hansen JE, Travis LD. Light scattering in planetary atmospheres. Space Sci Rev 1974;16:527–610.
[98] Aydın K. Centimeter and millimeter wave scattering from nonspherical hydrometeors. In: Mishchenko MI, Hovenier JW, Travis LD, editors. Light scattering by nonspherical particles: theory, measurements, and applications. San Diego: Academic Press; 2000. p. 451–79.
[99] Bringi VN, Chandrasekar V. Polarimetric, Doppler weather radar: principles and applications. Cambridge, UK: Cambridge University Press; 2001.
[100] Meischner P, editor. Weather radar: principles and advances applications. Berlin: Springer; 2004.
[101] Dubovik O, Sinyuk A, Lapyonok T, Holben BN, Mishchenko M, Yang P, et al. Application of spheroid models to account for aerosol particle nonsphericity in remote sensing of desert dust. J Geophys Res 2006;111:D11208.
[102] Mishchenko MI, Hovenier JW. Depolarization of light backscattered by randomly oriented nonspherical particles. Opt Lett 1995;20:1356–8.
[103] Chýlek P, Kiehl JT, Ko MKW. Narrow resonance structure in the Mie scattering characteristics. Appl Opt 1978;17:3019–21.
[104] Mishchenko MI, Travis LD, Mackowski DW. *T*-matrix computations of light scattering by nonspherical particles: a review. JQSRT 1996;55:535–75.
[105] Perry RJ, Hunt AJ, Huffman DR. Experimental determination of Mueller scattering matrices for nonspherical particles. Appl Opt 1978;17:2700–10.
[106] Shkuratov Yu, Bondarenko S, Kaydash V, Videen G, Muñoz O, Volten H. Photometry and polarimetry of particulate surfaces and aerosol particles over a wide range of phase angles. JQSRT 2007;106:487–508.
[107] Huckaby JL, Ray AK, Das B. Determination of size, refractive index, and dispersion of single droplets from wavelength-dependent scattering spectra. Appl Opt 1994;33:7112–25.
[108] Ray AK, Nandakumar R. Simultaneous determination of size and wavelength-dependent refractive indices of thin-layered droplets from optical resonances. Appl Opt 1995;34:7759–70.
[109] Huckaby JL, Ray AK. Layer formation on microdroplets: a study based on resonant light scattering. Langmuir 1995;11:80–6.

[110] Videen G, Li J, Chýlek P. Resonances and poles of weakly absorbing spheres. J Opt Soc Am A 1995;12:916–21.
[111] Tu H, Ray AK. Analysis of time-dependent scattering spectra for studying processes associated with microdroplets. Appl Opt 2001;40:2522–34.
[112] Zender CS, Talamantes J. Solar absorption by Mie resonances in cloud droplets. JQSRT 2006;98:122–9.
[113] Sassen K. Lidar backscatter depolarization technique for cloud and aerosol research. In: Mishchenko MI, Hovenier JW, Travis LD, editors. Light scattering by nonspherical particles: theory, measurements, and applications. San Diego: Academic Press; 2000. p. 393–416.
[114] Mishchenko MI, Sassen K. Depolarization of lidar returns by small ice crystals: an application to contrails. Geophys Res Lett 1998;25:309–12.
[115] Freudenthaler V, Homburg F, Jäger H. Optical parameters of contrails from lidar measurements: linear depolarization. Geophys Res Lett 1996; 23:3715–8.
[116] Schnaiter M, Benz S, Ebert V, Leisner T, Möhler O, Saunders RW, et al. Influence of particle size and shape on the backscattering linear depolarization ratio of small ice crystals. J Atmos Sci 2009 [submitted].
[117] Wagner R, Bunz H, Linke C, Möhler O, Naumann K-H, Saathoff H, et al., editors. Environmental simulation chambers: application to atmospheric chemical processes. Berlin: Springer; 2006. p. 67–82.
[118] Wagner R, Linke C, Naumann K-H, Schnaiter M, Vragel M, Gangl M, et al. A review of optical measurements at the aerosol and cloud chamber AIDA. JQSRT 2009;110 [this issue].
[119] Mishchenko MI, Travis LD, Kahn RA, West RA. Modeling phase functions for dustlike tropospheric aerosols using a shape mixture of randomly oriented polydisperse spheroids. J Geophys Res 1997;102:16831–47.
[120] Hill SC, Hill AC, Barber PW. Light scattering by size/shape distributions of soil particles and spheroids. Appl Opt 1984;23:1025–31.
[121] Bi L, Yang P, Kattawar GW, Kahn R. Single-scattering properties of triaxial ellipsoidal particles for a size parameter range from the Rayleigh to geometric-optics regimes. Appl Opt 2009;48:114–26.
[122] Zubko E, Kimura H, Shkuratov Y, Muinonen K, Yamamoto T, Okamoto H, et al. Effects of absorption on light scattering by agglomerated debris particles. JQSRT 2009;110:doi:10.1016/j.jqsrt.2008.12.006.
[123] Mugnai A, Wiscombe WJ. Scattering from nonspherical Chebyshev particles. 3. Variability in angular scattering patterns. Appl Opt 1989; 28:3061–73.
[124] Mishchenko MI, Macke A. How big should hexagonal ice crystals be to produce halos? Appl Opt 1999;38:1626–9.
[125] Lynch DK, Livingston W. Color and light in nature. Cambridge, UK: Cambridge University Press; 2001.
[126] Mishchenko MI, Rossow WB, Macke A, Lacis AA. Sensitivity of cirrus cloud albedo, bidirectional reflectance, and optical thickness retrieval to ice-particle shape. J Geophys Res 1996;101:16973–85.
[127] Liou KN, Takano Y, Yang P, Gu Y. Radiative transfer in cirrus clouds. In: Lynch DK, Sassen K, Starr D'OC, Stephens G, editors. Cirrus. New York: Oxford University Press; 2002. p. 265–96.
[128] Yang P, Liou KN. Single-scattering properties of complex ice crystals in terrestrial atmosphere. Contrib Atmos Phys 1998;71:223–48.
[129] Yang P, Liou KN. Light scattering and absorption by nonspherical ice crystals. Light Scattering Rev 2006;1:31–71.
[130] Borovoi AG, Kustova NV, Oppel UG. Light backscattering by hexagonal ice crystal particles in the geometrical optics approximation. Opt Eng 2006;44:071208.
[131] Macke A, Mueller J, Raschke E. Scattering properties of atmospheric ice crystals. J Atmos Sci 1996;53:2813–25.
[132] Macke A, Mishchenko MI, Cairns B. The influence of inclusions on light scattering by large ice particles. J Geophys Res 1996;101:23311–6.
[133] Labonnote C-L, Brogniez G, Buriez J-C, Doutriaux-Boucher M, Gayet J-F, Macke A. Polarized light scattering by inhomogeneous hexagonal monocrystals: validation with ADEOS–POLDER measurements. J Geophys Res 2001;106:12139–53.
[134] Khlebtsov NG. Optics and biophotonics of nanoparticles with a plasmon resonance. Quantum Electron 2008;38:504–29.
[135] Kahnert M, Sandvik AD, Biryulina M, Stamnes JJ, Stamnes K. Impact of ice particle shape on short-wave radiative forcing: a case study for an arctic ice cloud. JQSRT 2008;109:1196–218.
[136] Horvath H. Atmospheric light absorption—a review. Atmos Environ A 1993;27:293–317.
[137] Moosmüller H, Chakrabarty RK, Arnott WP. Aerosol light absorption and its measurement: a review. JQSRT 2009; 110 [this issue].
[138] Fuller KA, Malm WC, Kreidenweis SM. Effects of mixing on extinction by carbonaceous particles. J Geophys Res 1999;104:15941–54.
[139] Sorensen CM. Light scattering by fractal aggregates: a review. Aerosol Sci Technol 2001;35:648–87.
[140] Draine BT. The discrete dipole approximation for light scattering by irregular targets. In: Mishchenko MI, Hovenier JW, Travis LD, editors. Light scattering by nonspherical particles: theory, measurements, and applications. San Diego: Academic Press; 2000. p. 131–45.
[141] Yurkin MA, Hoekstra AG. The discrete dipole approximation: an overview and recent developments. JQSRT 2007;106:558–89.
[142] Mackowski DW, Mishchenko MI. Calculation of the *T* matrix and the scattering matrix for ensembles of spheres. J Opt Soc Am A 1996;13:2266–78.
[143] Klusek C, Manickavasagam S, Mengüç MP. Compendium of scattering matrix element profiles for soot agglomerates. JQSRT 2003;79/80:839–59.
[144] Liu L, Mishchenko MI. Effects of aggregation on scattering and radiative properties of soot aerosols. J Geophys Res 2005;110:D11211.
[145] Liu L, Mishchenko MI. Scattering and radiative properties of complex soot and soot-containing aggregate particles. JQSRT 2007;106:262–73.
[146] Liu L, Mishchenko MI, Arnott WP. A study of radiative properties of fractal soot aggregates using the superposition *T*-matrix method. JQSRT 2008;109:2656–63.
[147] Mackowski DW. A simplified model to predict the effects of aggregation on the absorption properties of soot particles. JQSRT 2006;100:237–49.
[148] West RA. Optical properties of aggregate particles whose outer diameter is comparable to the wavelength. Appl Opt 1991;30:5316–24.
[149] Horvath H, editor. Light scattering: Mie and more. JQSRT 2009;110 [this issue].
[150] Hough JH, editor. XI conference on electromagnetic and light scattering by nonspherical particles. JQSRT 2009;110 [in press].